



<b>Publication Year</b>	2024
<b>Acceptance in OA</b>	2025-03-28T14:34:31Z
<b>Title</b>	Fundamental physics measurements with Galileo FOC satellites and the Galileo for science project. II. A box wing for modeling direct solar radiation pressure and preliminaries orbit determinations
<b>Authors</b>	SAPIO, Feliciana, LUCCHESI, David, VISCO, Massimo, PERON, ROBERTO, LUCENTE, Marco, LEFEVRE, CARLO, CINELLI, MARCO, DI MARCO, Alessandro, FIORENZA, Emiliano, LOFFREDO, Pasqualino, MAGNAFICO, Carmelo, SANTOLI, Francesco, Vespe, Francesco
<b>Publisher's version (DOI)</b>	10.1103/PhysRevD.109.062005
<b>Handle</b>	<a href="http://hdl.handle.net/20.500.12386/36978">http://hdl.handle.net/20.500.12386/36978</a>
<b>Journal</b>	PHYSICAL REVIEW D
<b>Volume</b>	109

**Journal:** Physical Review D  
**Accession code:** DG13638  
**Article Title:** Fundamental physics measurements with Galileo FOC satellites and the Galileo for science project. II. A box wing for modeling direct solar radiation pressure and preliminaries orbit determinations  
**First Author:** Feliciana Sapio

**AUTHOR QUERIES - TO BE ANSWERED BY THE CORRESPONDING AUTHOR:**

The numbered items below correspond to numbers in the margin of the proof pages pinpointing the source of the question and/or comment. The numbers will be removed from the margins prior to publication.

**Q:** Please check that all references include complete titles.

Q1	Fourth Proof: Please check and verify closely to confirm all of the corrections have been incorporated properly throughout this Paper and also approve the Paper is ready to be published in its current form.
----	--

# Important Notice to Authors

***No further publication processing will occur until we receive your response to this proof.***

Attached is a PDF proof of your forthcoming article in *Physical Review D*. The article accession code is DG13638.

Please note that as part of the production process, APS converts all articles, regardless of their original source, into standardized XML that in turn is used to create the PDF and online versions of the article as well as to populate third-party systems such as Portico, Crossref, and Web of Science. We share our authors' high expectations for the fidelity of the conversion into XML and for the accuracy and appearance of the final, formatted PDF. This process works exceptionally well for the vast majority of articles; however, please check carefully all key elements of your PDF proof, particularly any equations or tables.


Figures submitted electronically as separate files containing color appear in color in the online journal.

However, all figures will appear as grayscale images in the print journal unless the color figure charges have been paid in advance, in accordance with our policy for color in print (<https://journals.aps.org/authors/color-figures-print>).

## Titles in References

The editors now encourage insertion of article titles in references to journal articles and e-prints. This format is optional, but if chosen, authors should provide titles for *all* eligible references. If article titles remain missing from eligible references, the production team will remove the existing titles at final proof stage.

## ORCIDs

Please follow any ORCID links () after the authors' names and verify that they point to the appropriate record for each author. Requests to add ORCIDs should be sent no later than the first proof revisions. If authors do not subsequently add/authenticate ORCIDs within seven business days, production of the paper will proceed and no further requests to add ORCIDs will be processed. See complete details regarding ORCID requests and ORCID verification at <https://journals.aps.org/authors/adding-orcids-during-proof-corrections>. If this paper is an Erratum or a Reply, the corresponding author's ORCID may be present if previously provided to APS, but no ORCIDs can be added at proof stage.

## Crossref Funder Registry ID:

Information about an article's funding sources is now submitted to Crossref to help you comply with current or future funding agency mandates. Crossref's Funder Registry (<https://www.crossref.org/services/funder-registry/>) is the definitive registry of funding agencies. Please ensure that your acknowledgments include all sources of funding for your article following any requirements of your funding sources. Where possible, please include grant and award ids. Please carefully check the following funder information we have already extracted from your article and ensure its accuracy and completeness:

- Agenzia Spaziale Italiana, FundRef ID <http://dx.doi.org/10.13039/501100003981> (IT/Repubblica Italiana)

## Other Items to Check

- Please note that the original manuscript has been converted to XML prior to the creation of the PDF proof, as described above. Please carefully check all key elements of the paper, particularly the equations and tabular data.
- Title: Please check; be mindful that the title may have been changed during the peer-review process.
- Author list: Please make sure all authors are presented, in the appropriate order, and that all names are spelled correctly.
- Please make sure you have inserted a byline footnote containing the email address for the corresponding author, if desired. Please note that this is not inserted automatically by this journal.
- Affiliations: Please check to be sure the institution names are spelled correctly and attributed to the appropriate author(s).

- Receipt date: Please confirm accuracy.
- Acknowledgments: Please be sure to appropriately acknowledge all funding sources.
- References: Please check to ensure that titles are given as appropriate.
- Hyphenation: Please note hyphens may have been inserted in word pairs that function as adjectives when they occur before a noun, as in “x-ray diffraction,” “4-mm-long gas cell,” and “*R*-matrix theory.” However, hyphens are deleted from word pairs when they are not used as adjectives before nouns, as in “emission by x rays,” “was 4 mm in length,” and “the *R* matrix is tested.”  
Note also that Physical Review follows U.S. English guidelines in that hyphens are not used after prefixes or before suffixes: superresolution, quasiequilibrium, nanoprecipitates, resonancelike, clockwise.
- Please check that your figures are accurate and sized properly. Make sure all labeling is sufficiently legible. Figure quality in this proof is representative of the quality to be used in the online journal. To achieve manageable file size for online delivery, some compression and downsampling of figures may have occurred. Fine details may have become somewhat fuzzy, especially in color figures. The print journal uses files of higher resolution and therefore details may be sharper in print. Figures to be published in color online will appear in color on these proofs if viewed on a color monitor or printed on a color printer.
- Overall, please proofread the entire *formatted* article very carefully. The redlined PDF should be used as a guide to see changes that were made during copyediting. However, note that some changes to math and/or layout may not be indicated.

## Ways to Respond














- **Web:** If you accessed this proof online, follow the instructions on the web page to submit corrections.
- **Email:** Send corrections to [aps-robot@luminad.com](mailto:aps-robot@luminad.com). Include the accession code DG13638 in the subject line.

## If You Need to Call Us

You may leave a voicemail message at +1.855.808.3897. Please reference the accession code and the first author of your article in your voicemail message. We will respond to you via email.

1  
2  
3  
4  
5  
6  
7  
8  
9  
10  
11  
12  
13  
14  
15  
16

## Fundamental physics measurements with Galileo FOC satellites and the Galileo for science project. II. A box wing for modeling direct solar radiation pressure and preliminaries orbit determinations

Feliciana Sapio <sup>1,2,3</sup>, David Lucchesi <sup>1,3,4,\*</sup>, Massimo Visco <sup>1,3</sup>, Roberto Peron <sup>1,3</sup>, Marco Lucente <sup>1,3</sup>,  
Carlo Lefevre <sup>1</sup>, Marco Cinelli <sup>1</sup>, Alessandro Di Marco <sup>1</sup>, Emiliano Fiorenza <sup>1</sup>, Pasqualino Loffredo <sup>1</sup>,  
Carmelo Magnafico <sup>1,3</sup>, Francesco Santoli <sup>1</sup> and Francesco Vespe <sup>5</sup>

<sup>1</sup>*Istituto Nazionale di Astrofisica (INAF), Istituto di Astrofisica e Planetologia Spaziali (IAPS),  
Via del Fosso del Cavaliere, 100, 00133 Roma, Italy*

<sup>2</sup>*Dipartimento di Fisica, Sapienza Università di Roma, Piazzale Aldo Moro 5, 00185 Roma, Italy*

<sup>3</sup>*Istituto Nazionale di Fisica Nucleare (INFN), Sezione di Tor Vergata,  
Via della Ricerca Scientifica 1, 00133 Roma, Italy*

<sup>4</sup>*Istituto di Scienza e Tecnologie della Informazione (ISTI), Consiglio Nazionale delle Ricerche (CNR),  
Via G. Moruzzi 1, 56124 Pisa, Italy*

<sup>5</sup>*Agenzia Spaziale Italiana (ASI), Centro di Geodesia Spaziale (CGS),  
Contrada Terlecchia, 75100 Matera, Italy*

(Received 16 July 2023; accepted 26 January 2024)

17  
18  
19  
20  
21  
22  
23  
24  
25  
26  
27  
28  
29  
30  
31  
32  
33  
34  
35  
36

This paper concerns the development of a first simplified model to take into account the perturbations produced by the nongravitational forces acting on the satellites of the Galileo FOC constellation and the corresponding first orbital determinations within the G4S\_2.0 project. G4S\_2.0 has a series of objectives in verifying the gravitational interaction in the weak field limit of the theory of general relativity, exploiting in particular the eccentricity of the orbits of some Galileo FOC satellites and the precise measurements that can be derived from the atomic clocks on board these satellites. The study focused on the model for the acceleration produced by direct solar radiation pressure on the satellites. This is the largest of all nongravitational perturbations. It is therefore necessary to build a sufficiently accurate model for it before being able to seriously consider smaller perturbation effects, such as those related to terrestrial radiation and thermal thrust effects. The work presents new aspects in the literature of navigation satellites. One of these is the determination of the effects in the Keplerian elements produced by the direct solar acceleration obtained from a box-wing model of the satellite. A second aspect is the comparison of these predictions in the orbital elements with the corresponding orbital residuals achieved from an orbit determination of the satellite. The study therefore highlights even more the importance of being able to improve the model of the perturbation originating from solar radiation in the field of global navigation satellite systems. This is very important if one wants to extract gravitational measurements from the orbit and clock-bias measurements of these satellites to verify the predictions of general relativity and compare them with those of alternative theories of gravitation.

DOI:

### I. INTRODUCTION

37  
38  
39  
40  
41  
42  
43  
44  
45  
46  
47

This paper mainly focuses on modeling direct solar radiation pressure (SRP) on the current constellation of ESA Galileo FOC satellites and constitutes the continuation of a work presented in this same issue [1]. In particular, we introduce the results obtained for the effects of SRP in the case of a box-wing model of the spacecraft obtained according to the metadata of ESA Galileo FOC satellites [2]. Although not new in the literature of the global navigation satellite systems (GNSS), our box-wing (BW) model presents, in its various applications, several

48  
49  
50  
51  
52  
53  
54  
55  
56

new aspects compared to what has already been published for the Galileo satellites, see for instance Bury *et al.* [3,4]. As explained in [1], this activity falls within the Galileo for Science (G4S\_2.0) project funded by the Italian Space Agency (ASI) [5–8]. The main goals of G4S\_2.0 are in the field of fundamental physics and exploit the relatively high eccentricity of the orbits of the Galileo GSAT0201 and GSAT0202 satellites and the accuracy of the on board atomic clocks, see [1] for details.

57  
58  
59  
60  
61

As said above, we are interested to model the effects of direct SRP on the Galileo FOC spacecraft. SRP represents the largest Non Gravitational Perturbation (NGP) on all GNSS satellites: about two orders of magnitude larger than the albedo perturbation, the second in magnitude. In fact,

\*david.lucchesi@inaf.it

as we have extensively illustrated in [1] (see Secs. II and IV therein), suboptimal modeling of SRP is currently the main source of error in determining the orbits of all GNSS satellites. Therefore, being able to improve the model for the SRP of Galileo satellites is extremely important for a number of different reasons, such as: (i) the use of the orbits and clocks of these satellites for the products of the International GNSS Service (IGS) [9], (ii) for more purely geophysical and geodetic applications within the global geodetic observing system (GGOS) [10], (iii) and for applications in the field of fundamental physics of current and next generation satellites [5,11,12].

In [1] (hereafter Paper I), we described, in particular, how we built our 3D model of the current Galileo FOC spacecraft (see Sec. XII A) and our BW model based on ESA metadata (see Sec. XII). In particular, we introduced what we called a simplified box-wing (S-BW) model and we provided its first applications within COMSOL [13] (see Section XII B). As explained in Paper I, the 3D model will be used to calculate the impact of the SRP—as well as that of the Earth’s radiation pressure—using a refined ray-tracing technique. This will only be possible once a much more in-depth characterization of the spacecraft is achieved than current knowledge based on presently available ESA metadata. This will be, in fact, our ultimate goal within G4S\_2.0. In this work we will present the results of our analytical S-BW model in the case of direct solar radiation.

Another object of our investigations, which will be presented in the second part of this work, concerns the orbital determination of the Galileo FOC satellites. In fact, after the improvement of the dynamic model, precise orbit determination (POD) represents the main tool with which to obtain, directly or indirectly, the various gravitational measurements of interest for our project. These measurements can directly concern the knowledge of the state vector of the satellites, as in the case of those related to relativistic precessions, or a better estimate of the clock-bias of the on board atomic clocks, as in the case of local position invariance tests or to set constraints in the presence of dark matter.

The rest of the paper is organized as follows. Section II defines the main characteristics of the Galileo FOC satellites that we have taken into consideration for our analyses. In this section the attitude law applied to these satellites is also introduced and described. Section III defines the model we have adopted for the interaction of incoming solar radiation with the surfaces of the spacecraft. The accelerations produced by SRP on satellites in elliptical orbits are calculated using the S-BW model. In particular, the acceleration results are provided in different reference frames and under different representations. Section IV exploits the results obtained for the accelerations in the Gauss reference frame to determine their effects in the orbital elements of the aforementioned satellites. In Sec. V, on the basis of a very simplified dynamical model,

we introduce our preliminary orbital determination for a Galileo satellite in elliptical orbit and for one in nominal orbit and we compare and discuss the obtained results. In particular, the orbital residuals of GSAT0201 have been computed and compared with the prediction of the S-BW model. In Sec. VI, we summarize the results obtained by interpreting them in terms of the further efforts to be made in the development of the dynamic model of the Galileo FOC satellites in order to achieve the fundamental physics objectives of G4S\_2.0. Finally, in Sec. VII our conclusions and recommendations are provided.

## II. THE GALILEO FOC SATELLITES

In the present work we will apply our S-BW model to the two aforementioned satellites GSAT0201 and GSAT0202 in elliptical orbit. The application of the model to GSAT0206 and GSAT0208, which are instead in their nominal (almost circular) orbit, will be provided later. The reason why our analyzes and simulations focus on these two different types of Galileo FOC satellites lies precisely in the nature of the different fundamental physics objectives of the G4S\_2.0 project.

As introduced in Paper I, elliptical orbits are particularly important for the modulation of the gravitational redshift signal and for the measurement of the total relativistic advancement of the satellite’s argument of pericenter. From the latter it is possible to measure the Schwarzschild and Lense-Thirring precession and, consequently, to place constraints on alternative theories of gravitation through their predictions on the relativistic advancement of the pericenter of the orbits [14–19]. Conversely, the satellites in nominal orbit (together with the two satellites in elliptical orbit), in particular the atomic clocks on board these satellites, will be useful for placing constraints on the possible presence of dark matter in the spherical halo in which our galaxy is immersed and for the possibility of detecting in future gravitational waves by the use of all the satellites of the constellation [20].

In both cases, an improved POD of these satellites with respect to the current state of the art is mandatory to achieve precise and accurate measurements in the field of fundamental physics. Therefore, as already underlined, one of our objectives in this direction is to improve the dynamic model of the orbits of satellites and, first of all, that of the nonconservative forces starting from the SRP. In Table I, some physical characteristics of the satellites and of their orbits are shown together with their identification numbers.

In addition to the satellite name [21], the Table shows two different numbers to identify each satellite: the pseudorandom noise (PRN) number and the space vehicle number (SVN). The mean Keplerian elements  $(a, e, i)$ , those at the reference date  $(\Omega_0, \omega_0, M_0)$  and their rate  $(\dot{\Omega}, \dot{\omega}, \dot{M})$ , are exactly those provided in the ESA metadata [22]. The slot indicates the orbital plane of each

TABLE I. Characteristics and orbital parameters of Galileo FOC satellites, mainly adapted from ESA Galileo metadata. The reference date for the satellites is November 21, 2016 at 00:00:00 UTC. Semi-major axis, eccentricity and inclination must be considered as mean values and not as obsculating elements. The metadata provides the indicated values for the mass of the satellites for December 2021 (see Sec. III for the mass values after the maneuvers of the satellites).

Type	Eccentric orbit	Nominal orbit	Nominal orbit
Name	GSAT0201, GSAT0202	GSAT0206	GSAT0208
PRN	E18, E14	E30	E08
SVN	E201, E202	E206	E208
Slot	Ext01, Ext02	A05	C07
Launch dates	August 22, 2014	September 11, 2015	December 17, 2015
Mass: $m$ (kg)	660.977, 662.141	707.735	709.138
Average cross-section: $A_{\odot}$ (m <sup>2</sup> )	13.210	13.210	13.210
Semi-major axis: $a$ (km)	27977.6	29599.8	29599.8
Eccentricity: $e$	0.162	0.0	0.0
Inclination: $i$ (°)	49.850	56.0	56.0
RAAN: $\Omega_0$ (°)	52.521	317.632	197.632
Argument of pericenter: $\omega_0$ (°)	56.198	0.0	0.0
Mean anomaly: $M_0$ (°)	316.069, 136.069	0.153	120.153
$\dot{\Omega}$ (°/d)	-0.03986760	-0.02764398	-0.02764398
$\dot{\omega}$ (°/d)	+0.03383184	0.0	0.0
$\dot{M}$ (°/d)	+667.86467481	+613.72253566	+613.72253566
Revolution period: $P$ (h)	12.94	14.08	14.08

171 satellite—A, B, C for satellites in nominal orbit and  
 172 “Extended” for satellites in elliptical orbit—with the  
 173 progressive number (up to a maximum of 8 for satellites  
 174 in nominal orbit) of the satellites in that plane. The average  
 175 cross section,  $A_{\odot}$ , is that seen from the Sun. It was  
 176 estimated by adding the average cross section of the bus  
 177 as seen from the Sun (2.390 m<sup>2</sup>) to the surface of the solar  
 178 panels (10.820 m<sup>2</sup>).

179 **A. The Galileo FOC attitude law**

180 The knowledge of the position of the spacecraft’s center-  
 181 of-mass (c.m.) [23] is not enough to describe the motion of  
 182 a satellite of complex shape and equipped with antennas  
 183 and motors, but it is also necessary to know the orientation  
 184 of the spacecraft with respect to the inertial space. In  
 185 Paper I, we briefly described the spacecraft attitude law.  
 186 In the following, we will provide useful details on the basis  
 187 of Galileo metadata and we will see the differences in the  
 188 application of this attitude law between satellites in  
 189 nominal orbit and those in elliptical orbit. In fact, in the  
 190 case of GNSS satellites the knowledge of their attitude is  
 191 very important for different reasons.

192 At first, because the navigation signals come from the  
 193 phase center of the antenna (PCA), whose position does not  
 194 coincide with that of the c.m. and, consequently, it is  
 195 necessary to refer these microwave measurements to the  
 196 c.m., i.e., the distance between the two points must be  
 197 known. This distance in general is not constant due to fuel  
 198 sloshing or mechanical movements of some Appendices, as  
 199 in the case of solar panels. Anyway, even assuming the  
 200 vector between these two points constant in magnitude,

its orientation in inertial space changes due to the attitude  
 law and its evolution needs to be known to correctly analyze  
 navigation signals [24,25]. The same considerations on the  
 microwave antennas and their PCA apply as well to the laser  
 retroreflector array (LRA) used for satellite laser ranging  
 (SLR). A third aspect is related to the so-called phase wind-  
 up effect. This is related to the knowledge of the observed  
 carrier phase, the latter depending on the relative orientation  
 between the spacecraft and its antennas with the transmitted  
 or received signals, which are right-handed circular polar-  
 ized: this is the phase wind-up effect [26,27]. Finally, and  
 this represents the aspect to which we are most interested  
 in this work, the modeling of the direct SRP finds its  
 implementation in the precise knowledge of the orientation  
 of the spacecraft body and of the solar panels with respect to  
 the incoming solar radiation [25,26].

For a GNSS spacecraft, the attitude is functional to the  
 navigation task and to the corresponding requirements  
 needed to guarantee it. In this regard, three drivers need  
 to be satisfied [27]:

- (1) The antenna boresight needs to be kept toward the  
 Earth’s center to provide the proper coverage and  
 signal strength to the on-ground receivers.
- (2) The solar panels need to maximise the received solar  
 radiation, by aligning them perpendicularly to the  
 Sun direction.
- (3) One of the spacecraft faces parallel to the antenna  
 boresight and to the solar panel rotation axis should  
 point opposite to the Sun, in order to ease the  
 thermal stability of atomic clocks (located close to  
 this position).

232 The result of these requirements is the implementation  
 233 of the yaw-steering (YS) mode, first implemented by  
 234 GPS [28] and later by most other constellations. Such an  
 235 approach is of course followed as well by the Galileo  
 236 satellites [29].

237 It is assumed a body reference frame with +Z-axis  
 238 aligned with the antenna boresight direction, +Y-axis  
 239 parallel to the rotation axis of the solar panels and the  
 240 -X-axis chosen so that the -X-panel is illuminated by the  
 241 Sun during nominal YS, while the +X-panel is oriented  
 242 toward deep space (the opposite for the other constella-  
 243 tion). In order to follow the three drivers, the attitude  
 244 requires a rotation of the spacecraft body about the  
 245 Earth pointing +Z-axis (yaw axis) as well as a rotation  
 246 of the solar panels about the +Y-axis (pitch axis) to be  
 247 perpendicular to the Sun.

248 The typical attitude for GNSS spacecrafts is that of a  
 249 nadir-pointing satellite, where the pitch and roll angles  
 250 vanish and the spacecraft attitude is fully described by the  
 251 yaw-angle  $\Psi$ ; this is the reason of the name *yaw-steering*  
 252 for the attitude mode. The yaw-angle  $\Psi$  is function of just  
 253 two angles: the Sun elevation  $\beta_{\odot}$  with respect to the orbital  
 254 plane and the position angle  $\mu$  of the satellite on the orbital  
 255 plane measured with respect to the midnight point or to the  
 256 noon point:

$$\Psi = \text{atan2}\left(\frac{-\tan\beta_{\odot}}{\sin\mu}\right), \quad (1)$$

258 where for the origin of  $\mu$  we followed the first convention  
 259 in agreement with [30], while  $\text{atan2}$  refers to the range  
 260  $(-\pi, +\pi)$  for the variability of the yaw-angle  $\Psi$ .

261 Following the ESA Galileo metadata, in the case of a  
 262 Galileo FOC spacecraft, Eq. (1) takes the following  
 263 expression:

$$\Psi = \text{atan2}\left(\frac{\hat{s}(t) \cdot \hat{n}(t)}{\hat{s}(t) \cdot (\hat{r}(t) \times \hat{n}(t))}\right), \quad (2)$$

264 where

- 265 (i)  $t$  is the current on-board computer time.
- 266 (ii)  $\hat{s}(t)$  is the Sun position unit vector.
- 267 (iii)  $\hat{r}(t)$  is the satellite position unit vector.
- 268 (iv)  $\hat{n}(t)$  is the orbit normal unit vector.

269 and all these unit vectors are in the Earth centered inertial  
 270 (ECI), J2000.0, reference frame.

271 However, the above law for the yaw-angle cannot be  
 272 applied at all times during the life of a spacecraft due to  
 273 technical limitations related to the performance of onboard  
 274 reaction wheels. This happens during the eclipse season  
 275 and, in particular, for small values of the  $\beta_{\odot}$  angle (above or  
 276 below the satellite's orbital plane) and near a collinear  
 277 condition for the vectors that identify the Sun and  
 278 the spacecraft with respect to the Earth, i.e., close to  
 279 "midnight" ( $\mu \simeq 0^\circ$ ) and close to "noon" ( $\mu \simeq 180^\circ$ ).  
 280

In these periods Galileo satellites (and GNSS in general) 281  
 have to perform fast yaw-slews to accomplish the yaw 282  
 angle change, i.e., an instantaneous rotation by  $180^\circ$  after 283  
 crossing the orbit midnight or noon position. 284

285 Furthermore, being such an attitude law based on the  
 286 use of solar sensors, the eclipse of the Sun in these  
 287 periods may result in non-nominal yaw angles during  
 288 limited periods of time. The result is that: (i) maneuvers at  
 289 noon and midnight positions depart from the nominal  
 290 attitude, causing a time delay between the current and the  
 291 nominal yaw angle, and (ii) additional manoeuvres are  
 292 needed to recover the nominal attitudes after the position  
 293 crossings. Moreover, a further drawback during these  
 294 phases is that the need to move the spacecraft with a  
 295 high yaw-rate, or close to it, can excite solar array  
 296 oscillations and/or propellant sloshing motion, inducing  
 297 at the same time c.m. displacements. This produces a  
 298 worst knowledge of the attitude, already degraded for the  
 299 transitions and, finally, in several related aspects, as  
 300 precise point positioning [31], tropospheric and clock  
 301 solutions [26] and in the overall POD [32]. We refer  
 302 to [27] for further details.

303 Consequently, in the case of the Galileo FOC satellites,  
 304 when the satellite and Sun position vectors are close to  
 305 collinearity, the following "modified" yaw steering law is  
 306 used:

$$\Psi_{\text{mod}}(t_{\text{mod}}) = 90^\circ \cdot \text{sign} + (\Psi_{\text{init}} - 90^\circ \cdot \text{sign}) \cdot \cos\left(\frac{2\pi}{T_0} t_{\text{mod}}\right), \quad (3)$$

where

- 307 (i)  $t_{\text{mod}}$  is the elapsed time since the switch over. 308
- 309 (ii)  $\Psi_{\text{init}}$  is the yaw-angle  $\Psi(t)$  at the time of the switch 310  
 over to the modified yaw profile. 311
- 312 (iii)  $\text{sign}$  is the sign of  $\Psi_{\text{init}}$ . 312

313 Therefore, close to orbit noon and midnight, Eq. (3), allows  
 314 to keep the yaw changing rate law compared to that  
 315 provided by Eq. (1). The period  $T_0 = 5656$  s corresponds  
 316 to about two times the maximum duration of the noon/  
 317 midnight maneuver.

318 As specified in the Galileo FOC metadata of ESA, the  
 319 switch over to the modified yaw steering law takes place  
 320 when all of the following conditions are met:

- 321 (i) The Sun elevation angle  $\beta_{\odot}$  is smaller than the  
 value  $\beta_0 = 4.1^\circ$ . 322
- 323 (ii) The current collinearity angle  $\epsilon$  is smaller than the  
 value  $\epsilon_0 = 10.0^\circ$ . 324
- 325 (iii) The collinearity angle for the previous epoch was  
 bigger than  $\epsilon_0$ . 326

327 The collinearity angle  $\epsilon$  is defined as follows:

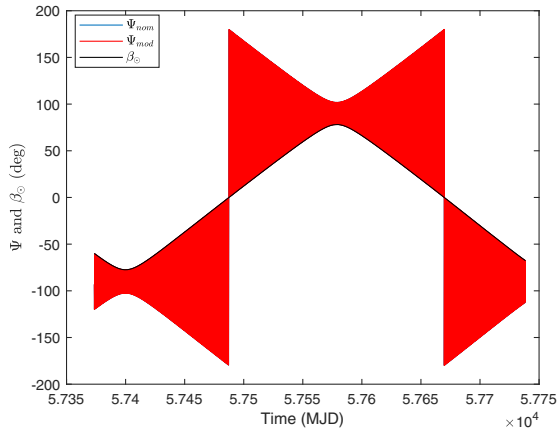
$$\begin{cases} \epsilon = \arccos(\hat{r} \cdot \hat{y}) & \text{if } \arccos(\hat{r} \cdot \hat{y}) \leq 90^\circ \\ \epsilon = 180^\circ - \arccos(\hat{r} \cdot \hat{y}) & \text{if } \arccos(\hat{r} \cdot \hat{y}) > 90^\circ, \end{cases} \quad (4)$$

329 where

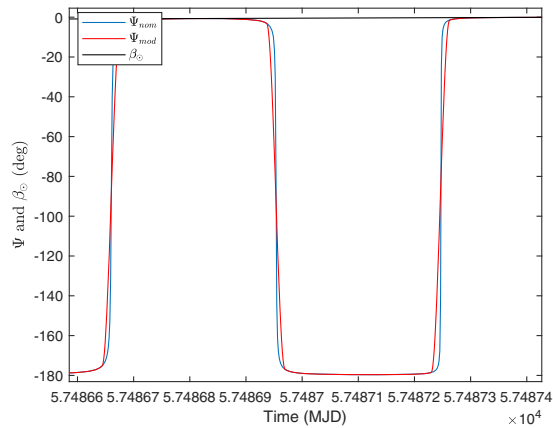
$$\begin{cases} \hat{x} = \hat{n} \times \hat{s} \\ \hat{y} = \hat{n} \times \hat{x} \end{cases} \quad (5)$$

330 In the following figures are shown the results for the  
 333 attitude law in the case of GSAT0208 on the basis of the  
 334 information provided in Table I and for a simulation period  
 335 of 1 year. In Fig. 1 it is shown the comparison of the  
 336 nominal and the modified yaw-steering law following ESA  
 337 metadata, i.e., Eqs. (2) and (3). The two laws perfectly  
 338 overlap outside the eclipse season, but show differences  
 339 near and during eclipses. Also shown is the change in the  
 340 height of the Sun,  $\beta_{\odot}$ , with respect to the orbital plane  
 341 during the simulated period.

342 The differences between the two attitude laws are  
 343 evident in Fig. 2, where the smoothest variation of the  
 344 modified law with respect to the nominal law is clear and  
 345 evident.



F1:1 FIG. 1. Nominal (blue) and modified (red) attitude law for  
 F1:2 GSAT0208. Two eclipse seasons are shown. The starting epoch  
 F1:3 corresponds to November 21, 2016. The black line defines the  
 F1:4 variation of the Sun's altitude with respect to the orbital plane in  
 F1:5 the period shown.



F2:1 FIG. 2. Detail of the Fig. 1 close to the first eclipse season.

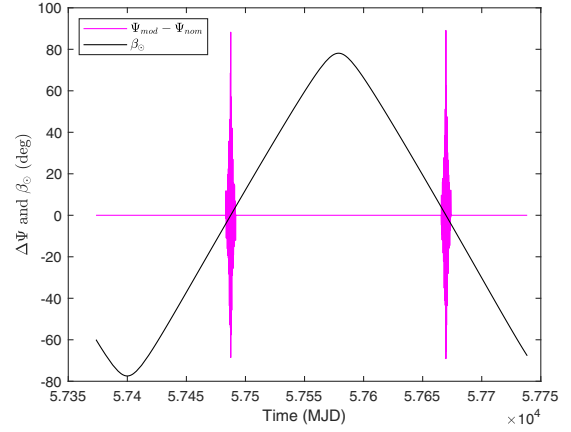


FIG. 3. Difference between the modified and nominal attitude laws for GSAT0208 together with the  $\beta_{\odot}$  angle variation.

F3:1  
 F3:2

Figure 3 shows the difference between the modified law  $\Psi_{\text{mod}}$  and the nominal law  $\Psi_{\text{nom}}$ . Clearly the differences are only along the eclipse seasons with the consequent nonorthogonality of the solar panels to the incoming solar radiation pressure.

346  
 347  
 348  
 349  
 350

It is important to underline that the attitude law described was designed for satellites in circular orbit, such as GNSS satellites in general, and not for satellites in elliptical orbit, such as GSAT0201 and GSAT0202. Currently, this attitude law is instead applied also to these satellites ([33]), and it is therefore not optimal for a profitable use of the tracking observations and for the PODs of these satellites during the eclipse season. In Figs. 4 and 5 the different behavior during the eclipses between GSAT0201, in elliptic orbit, and GSAT0208, in nominal (quasi circular) orbit, are shown.

351  
 352  
 353  
 354  
 355  
 356  
 357  
 358  
 359  
 360  
 361

The first figure provides the cosine of the angle between the solar panels normal and the direction of the incoming SRP. As can be derived, in the case of GSAT0208, the maximum fractional discrepancy from the orthogonality

362  
 363  
 364  
 365

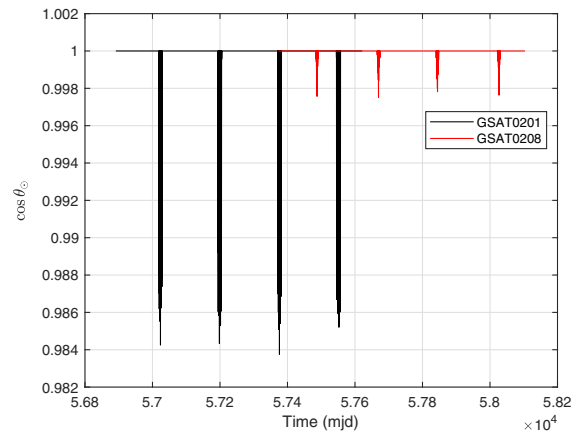
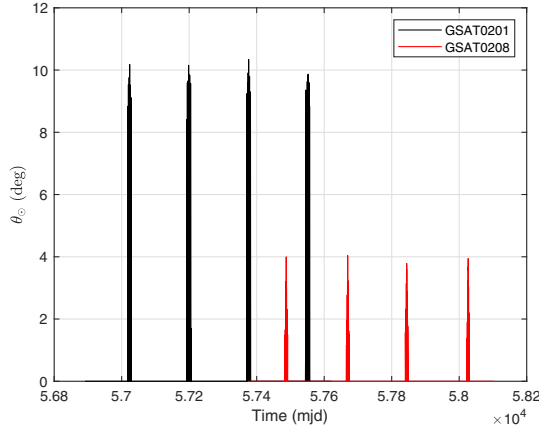


FIG. 4. Cosine of the angle between the normal to the solar panels and the direction of the incident solar radiation: comparison between GSAT0201 and GSAT0208.

F4:1  
 F4:2  
 F4:3



F5:1 FIG. 5. Angle between the normal to the solar panels and the  
 F5:2 direction of the incident solar radiation: comparison between  
 F5:3 GSAT0201 and GSAT0208.

366 condition to the solar panels for incoming solar radiation is  
 367 approximately 0.25%, increasing to 1.62% for GSAT0208.  
 368 The second figure shows that this maximum discrepancy  
 369 corresponds to an angle of about  $10^\circ$  for GSAT0201 and to  
 370 about  $4^\circ$  in case of GSAT0208.

371 Therefore, in order to make the most of the data useful to  
 372 the earth-segment from the satellites in elliptical orbit  
 373 during the eclipses, one should proceed with a variation  
 374 of the conditions linked to the modified attitude law  
 375 described by Eq. (3), in particular acting on the collinearity  
 376 angle  $\epsilon_0$ .

### 377 III. SPACECRAFT-SOLAR RADIATION 378 INTERACTION

379 In this section we apply the box-wing we have developed  
 380 to the modeling of the direct SRP. This model is fully  
 381 described in Section III B 4 of Paper I. We recall that it is a  
 382 box-wing model that we have defined “simplified” (S-BW),  
 383 since it is based on the current Galileo metadata [34], which  
 384 provide a very rough approximation of the real satellite.  
 385 The overall complex shape of the satellite bus—because of  
 386 the instrumentation of the face pointing to the Earth plus the  
 387 radiators on the other faces—and of the solar panels are  
 388 approximated by a parallelepiped plus symmetric wings, and  
 389 with average optical properties for five different materials,  
 390 already introduced in Table VI of Paper I. Equation (6)  
 391 provides the acceleration produced by the direct SRP on a  
 392 elementary surface  $dA$  of the spacecraft [35]:

$$394 \mathbf{d}\mathbf{a} = -\frac{\Phi_\odot}{mc} \left[ (1 - \rho) \hat{\mathbf{e}}_{\mathbf{D}} + 2 \left( \frac{\delta}{3} + \rho \cos \vartheta \right) \hat{\mathbf{n}} \right] dA |\cos \vartheta|, \quad (6)$$

395 where  $\Phi_\odot$  represents the solar irradiance,  $m$  the mass of the  
 396 satellite,  $c$  the speed of light, the unit vector  $\hat{\mathbf{e}}_{\mathbf{D}}$  is directed  
 toward the Sun from the spacecraft center of mass, and

397 finally  $\hat{\mathbf{n}}$  represents the unit vector normal to the surface and  
 398  $\vartheta$  the Sun zenith angle with respect to the surface normal,  
 399 such that  $\cos \vartheta = \hat{\mathbf{e}}_{\mathbf{D}} \cdot \hat{\mathbf{n}}$ . The optical coefficients  $\alpha$  (absorp-  
 400 tion),  $\rho$  (specular reflection), and  $\delta$  (diffusive reflection)  
 401 satisfies the condition:

$$\alpha + \rho + \delta = 1, \quad (7)$$

402 which shows that each surface  $dA$  behaves like a linear  
 403 combination of an ideal black body, a perfect mirror, and a  
 404 perfect diffuser. As explained in Paper I, we avoid the  
 405 approximation that assumes instantaneous thermal rera-  
 406 diation for the absorbed radiation, as suggested by [36]  
 407 and usually assumed in the GNSS literature [3,4,37]. We  
 408 will address this aspect in a work dedicated to thermal  
 409 effects. In fact, as highlighted in Paper I, these are  
 410 characterized by a plethora of effects of different origins  
 411 and act on the satellite with accelerations of the order  
 412 of  $10^{-10} \text{m/s}^2$  or less. They can therefore be taken into  
 413 serious consideration only after adequately modeling not  
 414 only direct solar radiation, but also terrestrial albedo and  
 415 infrared radiation pressure, see Table II.  
 416

417 In the following subsections we will present the results  
 418 obtained for the accelerations produced by the SRP  
 419 on the Galileo FOC satellite GSAT0201 characterized by  
 420 an elliptical orbit. The results obtained in the case of  
 421 GSAT0202 are provided in the Supplemental Material [39].  
 422 We will compare our results with those reported in the  
 423 literature and, in particular, with those of Bury *et al.* [3,4],  
 424 whenever possible. The simulations for the different  
 425 satellites were carried out over a two-year period starting  
 426 from the time of their launch, see Table I. An integration  
 427 step of 120 s has been used. The eclipses have been  
 428 modeled with a conical shadow model for a spherical Earth,  
 429 in such a way to consider penumbra effects [40]. In our  
 430 simulations we also considered the variation of the mass of  
 431 the satellites, when occurs, as reported by the international  
 432 laser ranging service (ILRS) [41], see Table III.  
 433

434 Table IV provides the Keplerian orbital elements of the  
 435 satellites that we computed from the precise orbits of ESA  
 436 determined at ESOC. This provides orbits more accurate  
 437 than those reported in the ESA Galileo Metadata, which  
 438 seem approximate or physically implausible for several  
 439 orbital elements and their rates. Therefore, the satellites  
 440 state-vector (position and velocity) calculated in the ter-  
 441 restrial rotating reference frame (sp3c files: Extended  
 442 Standard Product-3 format) have been transformed, on  
 443 the basis of current IERS Conventions [42]—i.e., taking  
 444 into account for polar motion, precession and nutation—  
 445 from the rotating frame to the J2000.0 inertial one. This  
 446 state-vector was finally transformed into the corresponding  
 447 six Keplerian elements. Finally, from the temporal evolu-  
 448 tion of the elements we estimated their corresponding rate.  
 449 We have kept from the Galileo metadata only the informa-  
 450 tion relating to the mean anomaly  $M$  of the two satellites.

TABLE II. Main nongravitational accelerations (S.I. units) on a Galileo FOC satellite. The symbol ( $\dots$ ) means that the acceleration is negligible, while the symbol (NA) means that the acceleration is currently unknown (not available), since it has not yet been evaluated. We refer to Paper I for more details.

Physical effect	Formula	Parameter [S.I. units/adim]	Galileo FOC
Direct SRP	$C_R \frac{A}{m} \frac{\Phi_\odot}{c}$	$\Phi_\odot = 1360.8$	$1.0 \times 10^{-7}$
Earth's Albedo	$2 \frac{A}{m} \frac{\Phi_\oplus}{c} A_\oplus \frac{\pi R_\oplus^2}{4\pi r^2}$	$A_\oplus \approx 0.3$	$7.0 \times 10^{-10}$
Earth's infrared radiation	$\frac{A}{m} \frac{\Phi_{IR}}{c} \frac{R_\oplus^2}{r^2}$	$\Phi_{IR} \approx 240$	$1.1 \times 10^{-9}$
Neutral drag	$\frac{1}{2} C_D \frac{A}{m} \rho V^2$	$C_D, \rho$	$\dots$
Charged drag	[38], Chap. 5	Species densities, floating potential	$\neg$
Power from antennas	$\frac{P}{mc}$	$P \simeq 265$	$1.2 \times 10^{-9}$
Thermal effect solar panels	$\frac{2}{3} \frac{\sigma A}{c m} (\epsilon_1 T_1^4 - \epsilon_2 T_2^4)$	$\epsilon_1 \simeq \epsilon_2 \approx 0.8, T_1 \simeq 317, T_2 \simeq 318$	$1.9 \times 10^{-10}$
Y-bias	$Y_0$ : empirical acceleration	$Y_0$	$7.0 \times 10^{-10}$
Poynting-Robertson	$\frac{1}{4} \frac{A}{m} \frac{\Phi_\odot}{c} \frac{R_\oplus^2}{r^2} \frac{v}{c}$	$\Phi_\odot = 1360.8$	$1.9 \times 10^{-14}$
Solar Yarkovsky-Schach	$\frac{16}{9} \frac{A}{m} \frac{\epsilon \sigma}{c} T_0^3 \Delta T$	$\epsilon, T_0, \Delta T$	$\neg$
Earth Yarkovsky	$0.41 \frac{4}{9} \frac{A}{m} \frac{c \Phi_{IR} f_0}{ac} \frac{R_\oplus^2}{r^2}$	$\Phi_{IR}, f_0, \alpha$	$\neg$

TABLE III. Mass values for Galileo satellites FOC GSAT0201 (E18) and GSAT0202 (E14). These values for satellite masses are current as of December 20, 2022.

Satellite	Time interval	Mass [kg]	Time interval	Mass [kg]
GSAT0201	August 22, 2014	660.977		
GSAT0202	August 22, 2014 to July 30, 2015	662.646	July 31, 2015 to onward	662.141

**A. Long-term analysis of the SRP accelerations: GSAT0201**

Figure 6, shows the variation of the Sun's height  $\beta_\odot$ , over the 2-year period of the current simulation, with respect to the orbital plane of GSAT0201 together with the modified and nominal attitude law for  $\Psi$ , as described in the Galileo metadata.

It is precisely the evolution over time of the satellite attitude law, characterized by a long-term evolution mainly linked to the satellite's draconic year, and by higher-frequency evolutions, mainly at the orbital period of the satellite, which shapes the evolution over time of the perturbation linked to solar radiation.

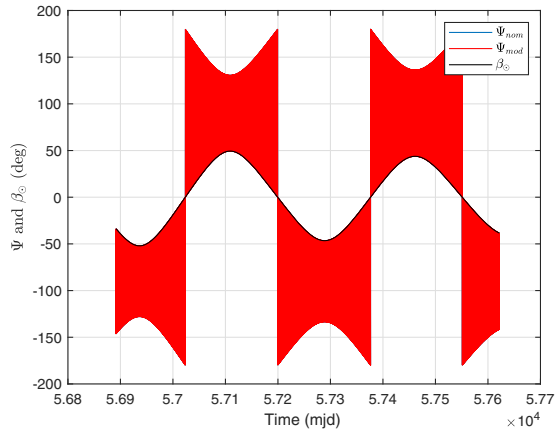
The following figures show the impact of the accelerations due to the direct SRP in the case of the GSAT0201 satellite approximated with the S-BW model. The results are provided in three different frames of the satellite, see Fig. 7.

Figure 8 shows the acceleration in the DYB frame of the spacecraft, which is also known as the Sun-satellite-Earth (SSE) reference frame. The D-axis is defined by the unit vector  $\hat{\mathbf{e}}_D$  already introduced,  $\hat{\mathbf{e}}_Y$  is the unit vector along the spacecraft solar panel axis and defines the Y-axis, finally  $\hat{\mathbf{e}}_B = \hat{\mathbf{e}}_D \times \hat{\mathbf{e}}_Y$  defines a right-handed reference system and the corresponding B-axis. The overwhelming contribution of the acceleration along the D-axis is due to the interaction of direct SRP with the solar panels which, according to the attitude law described in Sec. II A, are always orthogonal to the solar rays except in periods characterized by eclipses. To a lesser extent, the interaction of solar radiation with the faces of the bus of the spacecraft contributes once the different contributions are projected along the D-axis.

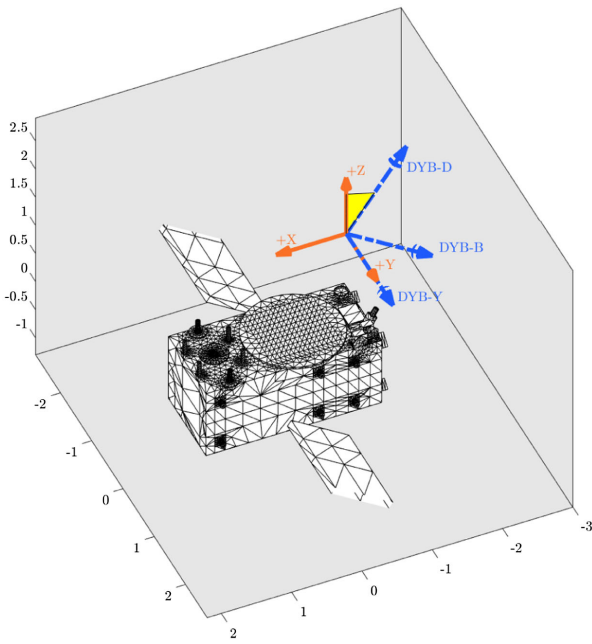
As we can see from this figure, the maximum accelerations (in absolute value) along the D-axis are about two orders of magnitude greater than the accelerations along the B-axis. Indeed, the behavior of the acceleration along the

TABLE IV. Orbital elements for the Galileo FOC satellites GSAT0201 (E18) and GSAT0202 (E14) estimated from the Precise Orbits of ESOC. The reference date for the satellites is November 21, 2016 at 00:00:00 UTC.

Satellite	$a$ [m]	$e$	$I$ [°]	$\Omega$ [°]	$\omega$ [°]	$M$ [°]
GSAT0201	27978099.66	0.1604	50.369	53.505	50.184	316.069
				-0.04000414086 [°/d]	+0.04910776939 [°/d]	+667.909221051 [°/d]
GSAT0202	27977624.83	0.1608	50.309	52.459	52.086	136.069
				-0.04002923721 [°/d]	+0.04784293004 [°/d]	+667.909221051 [°/d]



F6:1 FIG. 6. GSAT0201 (E18): nominal (blue) and modified (red)  
 F6:2 attitude law. Four eclipse seasons are shown. The starting epoch  
 F6:3 corresponds to August 23, 2014. The black line defines the  
 F6:4 variation of the Sun's altitude with respect to the orbital plane in  
 F6:5 the period shown.



F7:1 FIG. 7. Representations of the DYB and XYZ reference frames  
 F7:2 of the spacecraft. The yellow sector highlights the direction of the  
 F7:3 Sun along the +D axis compared to the +Z direction which  
 F7:4 instead points toward the Earth.

486 D-axis is very close to the behavior of the absolute value of  
 487 the direct SRP on the S-BW model, see Fig. 9. Concerning  
 488 the behavior of the acceleration along the Y-axis, this is the  
 489 same as the one shown in Fig. 13: it is nonzero only during  
 490 the eclipse season in this approximation for the orientation  
 491 of the solar panels with respect to the incoming solar  
 492 radiation pressure.

493 Figure 10, shows the behavior of the direct SRP  
 494 acceleration in the Gauss comoving frame ( $\hat{r}, \hat{t}, \hat{w}$ ). In this

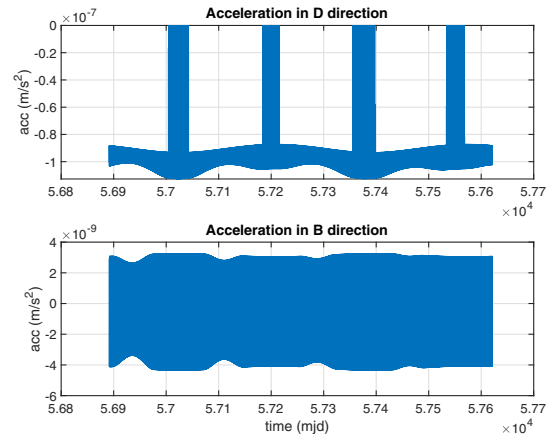


FIG. 8. GSAT0201 (E18): acceleration due to direct SRP along  
 the D (top) and B (bottom) directions.

F8:1  
 F8:2

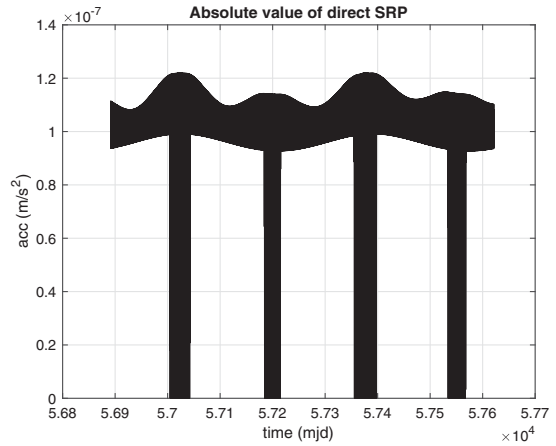


FIG. 9. GSAT0201 (E18): absolute value of the acceleration  
 due to direct SRP.

F9:1  
 F9:2

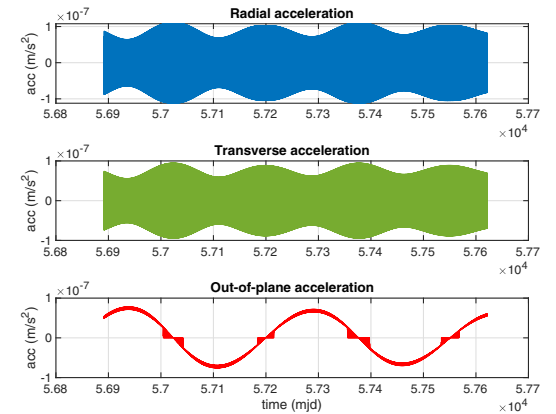


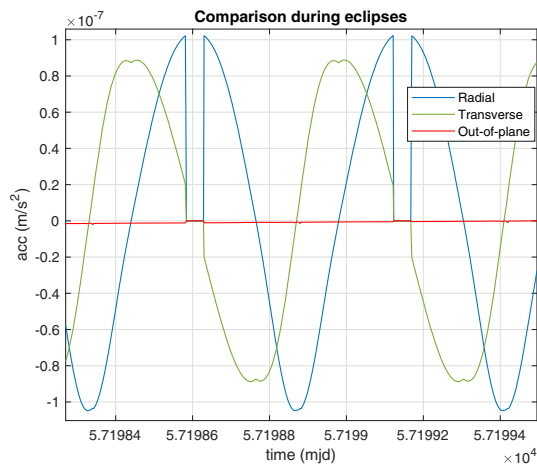
FIG. 10. GSAT0201 (E18): acceleration due to direct SRP  
 along the directions of the Gauss comoving frame.

F10:1  
 F10:2

495 frame corotating with the satellite revolution around the  
 496 Earth, the radial direction ( $\hat{r}$ ) is identified by the direction  
 497 from the Earth's center of mass to the satellite center of  
 498 mass. The out-of-plane or cross-track direction ( $\hat{w}$ ) is  
 499 identified by the obsculating angular momentum direction.  
 500 Finally, the transverse direction ( $\hat{t}$ ) is defined in such a way  
 501 to define a right-handed reference system:  $\hat{t} = \hat{w} \times \hat{r}$ .  
 502 For our purposes, the introduction of the Gauss reference  
 503 frame is important to express the perturbing effects of the  
 504 modeled SRP in the so-called Gauss perturbing equations.  
 505 This will allow us to estimate the impact of the disturbance  
 506 effects on the orbital elements, see Sec. IV.

507 As we can see from Fig. 10, the radial  $R$  and transverse  $T$   
 508 accelerations have a similar behavior and magnitude. The  
 509 maximum values for the out-of-plane  $W$  acceleration are a  
 510 little smaller and its long-term behavior is clearly modu-  
 511 lated by the variation of the solar height with respect to the  
 512 orbital plane. This long-term modulation is also present for  
 513 the other two components, but for these components the  
 514 modulation of the acceleration at the orbital period assumes  
 515 a clear and evident importance. In Figs. 11 and 12 we  
 516 compare these three components of the direct SRP in two  
 517 very different conditions for the Sun height  $\beta_{\odot}$ : during a  
 518 few eclipses (where the solar height is very close to zero)  
 519 and far way from the eclipses (where the solar height is  
 520 very close to its maximum value). Obviously, in the first  
 521 case the out-of-plane component of the SRP acceleration  
 522 is practically zero and its effects on the orbital elements  
 523 are fully negligible. Conversely, in the second case the  
 524 out-of-plane component is almost constant and greater  
 525 than the other two components. Finally, the radial and  
 526 transverse components have similar behavior in the two  
 527 cases, as already anticipated.

528 Finally, Fig. 13 shows the components of direct SRP  
 529 acceleration in the spacecraft frame already introduced in  
 530 Sec. II A, the  $XYB$  frame. The  $Y_B$ -axis coincides with the  
 531 solar panel axis  $Y$ -axis of the  $DYB$  frame and the  $Z_B$ -axis



F11:1 FIG. 11. GSAT0201 (E18): components of the Gauss per-  
 F11:2 turbing acceleration due to direct SRP during eclipses.

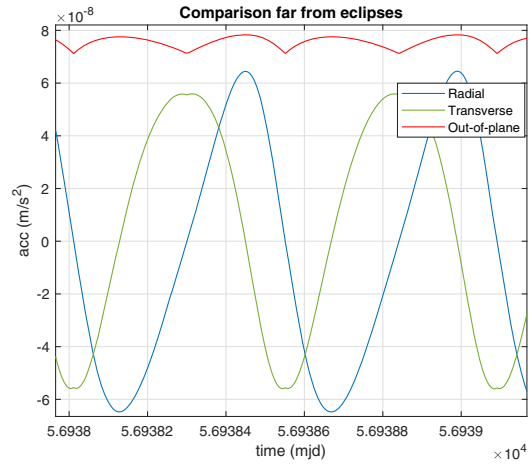


FIG. 12. GSAT0201 (E18): components of the Gauss per- F12:1  
 turbing acceleration due to direct SRP far from eclipses. F12:2

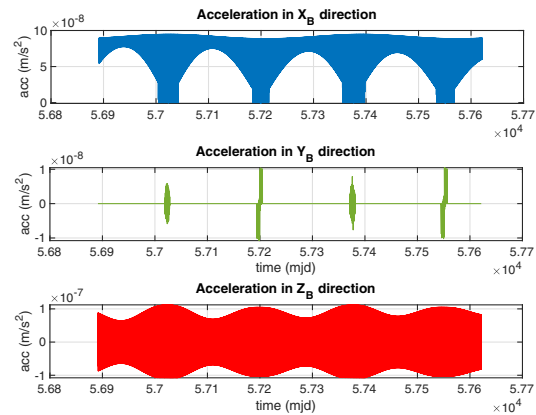


FIG. 13. GSAT0201 (E18): acceleration due to direct SRP F13:1  
 along the spacecraft body axes. F13:2

532 is nadir pointing and opposite to the radial direction axis  
 533 of the Gauss frame. The  $X_B$ -axis completes the right  
 534 handed frame:  $\hat{X}_B = \hat{Y}_B \times \hat{Z}_B$ . In practice, the  $XYZ$   
 535 frame coincides with the mechanical reference frame  
 536 introduced in Paper I.

537 This reference frame is interesting to consider in view of  
 538 the possible on-board installation of an accelerometer in a  
 539 next generation of Galileo satellites. This is one more goal  
 540 of the G4S\_2.0 project. In fact, the  $XYZ$  frame represents  
 541 the reference integral with the satellite on which to orient  
 542 the three axes of the accelerometer. An accelerometer of the  
 543 right sensitivity and measurement band would in fact  
 544 provide a direct measurement of the various nongravita-  
 545 tional and inertial accelerations to which the satellite is  
 546 subjected. Therefore, an on-board accelerometer will con-  
 547 tribute improving the satellites POD, also using its mea-  
 548 surements in synergy with the new models for NGPs.

549 In the next subsections we will deepen the description of  
 550 the results obtained according to two different representa-  
 551 tions for the accelerations produced by direct solar radiation.

### 1. Synoptic view of the accelerations

After introducing a representation in the time domain of the components of the acceleration produced by the SRP according to three different reference systems, in this section we are interested to introduce and discuss the representation of the components of the SRP according to two other different approaches. The first is a synoptic representation of the acceleration in the plane  $(\Delta u, \beta_\odot)$ , where  $\Delta u = u - u_\odot$  is the difference between the argument of latitude  $u$  of the satellite with respect to that of the Sun  $u_\odot$ . From the practical point of view,  $\Delta u$  represents the azimuth of the satellite direction in the orbital plane with respect to the projection of the Sun direction in that plane. The second approach is instead based on the spectral analysis of the different components of the acceleration produced by the SRP, see Sec. III A 2. Both approaches are important to characterize accelerations more fully, as we will see, and to allow us to improve their modeling and, consequently, the final orbital determination of the satellite.

In Figs. 14(a) and 14(b) the synoptic representation of the accelerations produced by the direct SRP along the D and B directions are shown. We have restricted the representation to the first 200 days of our simulation, so as to contain a single excursion in the height of the Sun between its minimum and its maximum (whose periodicity is approximately 183 days). This allows us not to report on the plane the further acceleration variations linked to the variation—between the successive maximum and minimum values, of the height of the Sun due to the precession of the orbital plane—accelerations which would tend to stratify on the previous values “dirtying” the representation itself. The color bar provides the accelerations values in  $\text{m/s}^2$ .

In the case of the Figs. 14(a) and 14(b), the trend of the values traced for the accelerations depends on the variable geometry of the SSE reference frame, which is influenced by the variation of the solar height with respect to the orbital plane and its distance from the satellite, as well as by the different attitude of the spacecraft with respect to the Earth and the Sun.

This type of representation for accelerations is more useful than the one previously reported in the time domain when one wants to highlight the variations of the dynamic perturbation model with respect to a basic model taken as a reference. As we highlighted in Paper I, our ultimate goal is to develop a FEM for the Galileo-FOC and apply an *ad hoc* raytracing technique to calculate the different perturbative accelerations, starting from the direct SRP.

As a possible example of this aspect, we can compare our results in the D and B directions with the corresponding results obtained in [4]. We recall that these authors modeled the absorbed radiation assuming that it is instantaneously reemitted back to space according to Lambert’s law, see Eq. (7) of Paper I. The authors assumed that this will make a difference for the bus but not for the solar panels, since

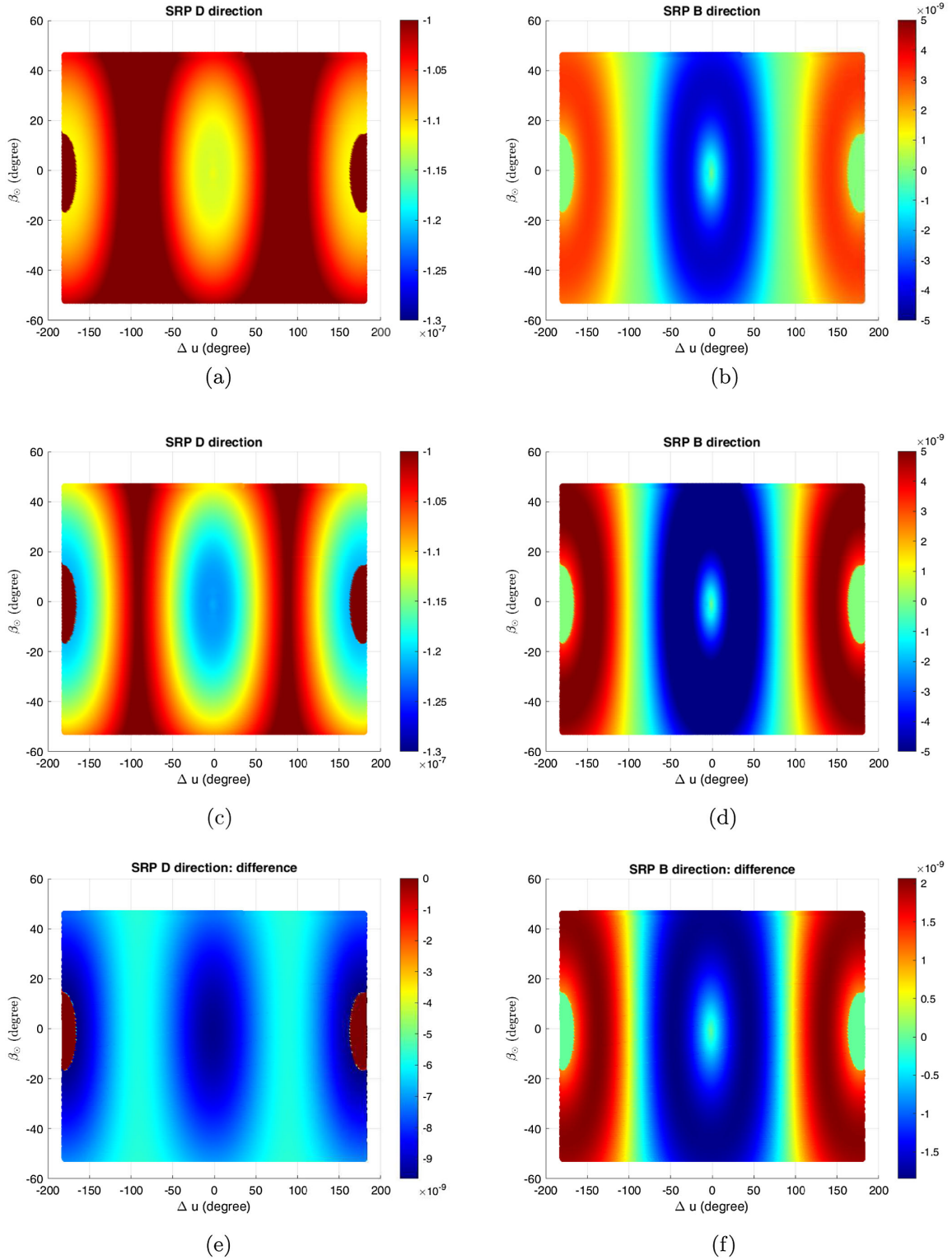
they assumed the same temperature for the front and back sides of the panels. For geometric reasons, we expect this further acceleration to have a greater impact along the D direction and a lesser impact along the B direction, although not zero. Indeed, if we compare our Figs. 14(a) and 14(b) with Fig. 2 of [4], respectively (bottom left) and (bottom right), for the Galileo-FOC E18 satellite, we note that the most evident discrepancies occur along the D direction. Conversely, if we include in our model, i.e., in Eq. (6), the immediate thermal re-radiation to space of the absorbed radiation, we obtain the two representations of Figs. 14(c) and 14(d) for the accelerations along the D and B directions. In this case our Fig. 14(d) is practically indistinguishable from that of [4], while Fig. 14(c) still shows some differences related to the different attitude law modeled for the satellite: in [4] a perfect orthogonality between the solar panels with the direction of the incoming solar radiation has been assumed, this is reflected in evident differences when  $\beta_\odot$  is close to zero.

In Figs. 14(e) and 14(f) we show the differences in the synoptic representation due to the contribution of the immediate thermal re-radiation of the absorbed radiation. Naturally, as already highlighted in the above discussion, the major differences occur in the case of direction D, see the acceleration values on the scale of the color bar.

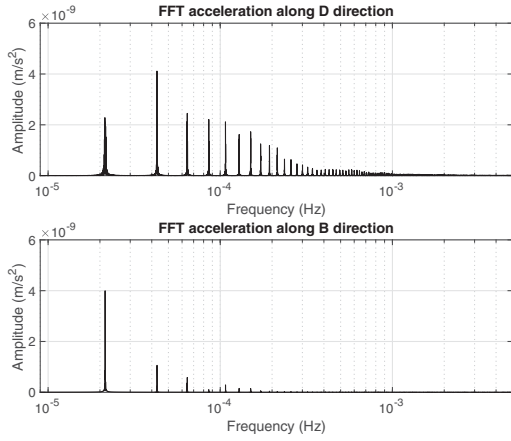
### 2. Spectral analysis of the accelerations

Figure 15 shows the different behavior for the two components of the acceleration along the D and B directions in the frequency domain. The fast Fourier transform (FFT) has been computed on the 2-year period of the analysis, but long-term effects (low frequencies) were not represented in the figure. The acceleration amplitude in the two components is expressed in terms of the frequency in Hz in a semilogarithmic scale. The spectral lines are at the orbital revolution frequency  $f_{\text{orb}} \simeq 2.15 \times 10^{-5}$  Hz and its integer multiples, and greater along the D direction, in accordance with the values reported in Figs. 8, 14(a), and 14(b). Indeed, as was reasonable to expect, the spectrum is characterized by larger amplitudes along the D direction—see for example the lines at 2, 3 and 4 times the orbital frequency—due to the attitude law and to the nadir pointing of the satellite, which make the contribution of the satellite bus more relevant. In these cases, the amplitudes of the acceleration are comparable at different frequencies: between  $2 \times 10^{-9}$   $\text{m/s}^2$  and  $4 \times 10^{-9}$   $\text{m/s}^2$ . Conversely, in the case of acceleration along the B direction, the amplitudes of acceleration at higher frequency are much smaller than that at orbital frequency.

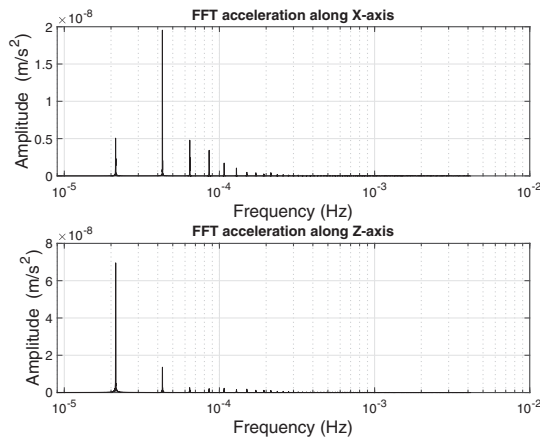
Figure 16 shows the different behavior for the two components of the acceleration along the X and Z directions in the frequency domain. The X-component of the SRP acceleration is dominated by a line at twice of the orbital frequency with an amplitude of about  $1.95 \times 10^{-8}$   $\text{m/s}^2$ , while the Z-component (or radial component) is dominated by a line at the orbital frequency with



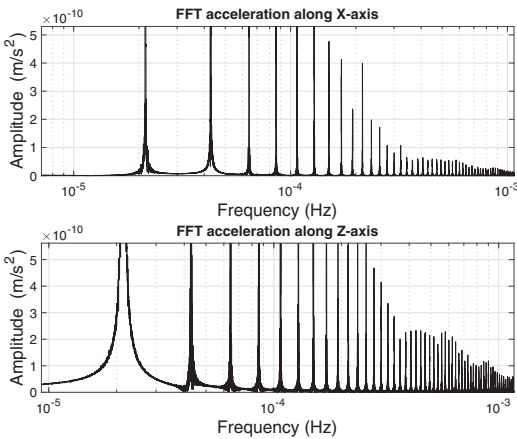
F14:1 FIG. 14. GSAT0201 (E18): synoptic view of the acceleration due to direct SRP along the D and B directions. (a) GSAT0201 (E18):  
 F14:2 synoptic view of the acceleration due to direct SRP along the D direction; (b) GSAT0201 (E18): synoptic view of the acceleration due to  
 F14:3 direct SRP along the B direction; (c) GSAT0201 (E18): synoptic view of the acceleration due to direct SRP along the D direction in case  
 F14:4 of immediate thermal re-radiation; (d) GSAT0201 (E18): synoptic view of the acceleration due to direct SRP along the B direction in  
 F14:5 case of immediate thermal re-radiation; (e) GSAT0201 (E18): differences in the synoptic representation of the acceleration due to direct  
 F14:6 SRP along the D direction with and without thermal re-radiation; and (f) GSAT0201 (E18): differences in the synoptic representation of  
 F14:7 the acceleration due to direct SRP along the B direction with and without thermal re-radiation.



F15:1 FIG. 15. GSAT0201 (E18): spectral analysis of the SRP  
 F15:2 accelerations along the D (top) and B (bottom) directions.



F16:1 FIG. 16. GSAT0201 (E18): spectral analysis of the SRP  
 F16:2 accelerations along the X (top) and Z (bottom) directions.



F17:1 FIG. 17. GSAT0201 (E18): spectral analysis of the SRP  
 F17:2 accelerations along the X (top) and Z (bottom) directions.  
 F17:3 Particular of Fig. 16.

TABLE V. GSAT0201 (E18). Acceleration values (in units of  $10^{-9} \text{ m/s}^2$ ) for the D, B, X, and Z components of the SRP for the first five spectral lines.

Component	$f_{\text{orb}}$	$2f_{\text{orb}}$	$3f_{\text{orb}}$	$4f_{\text{orb}}$	$5f_{\text{orb}}$
D	2.28	4.12	2.45	2.21	2.12
B	4.00	1.06	0.58	0.10	0.29
X	5.05	19.54	4.78	3.43	1.72
Z	69.53	13.58	2.62	2.11	2.30

an amplitude of about  $6.95 \times 10^{-8} \text{ m/s}^2$ . In the case of  
 X-component, the line at the orbital frequency has an  
 amplitude of about  $5.0 \times 10^{-9} \text{ m/s}^2$ , while for the  
 Z-component the line at twice of the orbital frequency  
 has an amplitude of about  $1.36 \times 10^{-8} \text{ m/s}^2$ .

To find accelerations with amplitude of the order of  
 few times  $10^{-10} \text{ m/s}^2$ , comparable to the main effects of  
 thermal origin (see Table II), periodic effects with fre-  
 quency greater than  $6 \times 10^{-5} \text{ Hz}$  must be considered, see  
 Fig. 17 and Table V.

Table V summarizes, for the first five spectral lines, the  
 values of the amplitudes found for the four components of  
 the direct SRP acceleration analyzed here.

The results obtained in terms of spectral lines are  
 congruent with those shown in [4], although the represen-  
 tation is different, since these authors expressed the  
 amplitudes as a function of the orbital revolutions and  
 not of the frequency in Hz. The amplitudes of the different  
 lines are slightly different in the cited paper mainly because  
 are calculated over a different (smaller) time length.

In Fig. 18 also the long-period effects of SRP in the X  
 and Z directions are shown. Obviously, the low-frequency  
 effects are not as evident as the high-frequency ones, since  
 the timespan of the analysis is not long enough to  
 adequately resolve them.

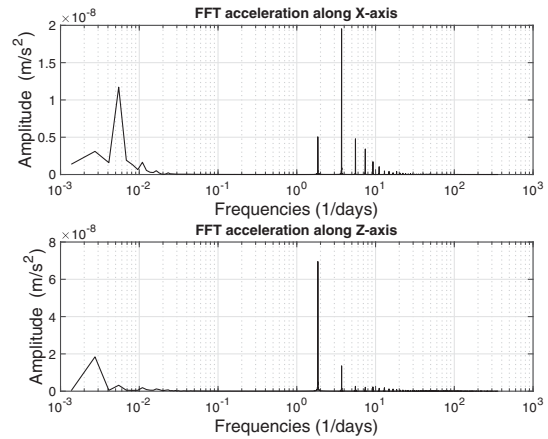


FIG. 18. GSAT0201 (E18): spectral analysis of the SRP  
 accelerations along the X (top) and Z (bottom) directions also  
 showing the long-period effects of direct SRP.

686 **IV. LONG-TERM ANALYSES: ORBITAL EFFECTS**

687 In this section we are interested to introduce an estimate  
 688 of the long-term effects on satellite orbits produced by  
 689 direct solar radiation pressure on the basis of the previously  
 690 introduced S-BW model. We want to underline that the  
 691 BW model, although it is not a good approximation of the  
 692 satellite behavior as far as short-term effects are concerned,  
 693 is nevertheless useful for delineating the long-term pertur-  
 694 bative effects of direct SRP.

695 This will provide us with useful information regarding  
 696 some measures of fundamental physics, such as the  
 697 relativistic precessions of the orbits and the consequent  
 698 constraints that can be placed on some alternative theories  
 699 of gravitation, i.e., alternative to general relativity in their  
 700 predictions.

701 The most natural way to proceed in this direction is to  
 702 exploit the accelerations produced by the SRP in the Gauss  
 703 triad through the corresponding perturbation equations of  
 704 the osculating elements. In particular, Gauss' perturbation  
 705 equations describe the variations of the Keplerian elements  
 706 under the action of a perturbing acceleration of any origin,  
 707 i.e., due to conservative or nonconservative forces. In the  
 708 following the Gauss equations for the osculating ellipse  
 709 are shown [35]:

$$\frac{da}{dt} = \frac{2}{n\sqrt{1-e^2}} [T + e(T \cos f + R \sin f)] \quad (8)$$

710 
$$\frac{de}{dt} = \frac{\sqrt{1-e^2}}{na} [R \sin f + T(\cos f + \cos E)] \quad (9)$$

713 
$$\frac{dI}{dt} = \frac{W}{H} r \cos(\omega + f) \quad (10)$$

715  
 745

$$\frac{d\eta}{dt} = R \left[ \frac{\cos E}{nae(1-e^2)} - \frac{\sqrt{1-e^2} \sin f \sin E}{na} + \frac{2r}{na^2} \right] + T \left[ \frac{\sqrt{1-e^2} \sin E}{nae} \left( \frac{a}{r} - 1 \right) + \frac{\sqrt{1-e^2}}{na} \sin E (\cos f + \cos E) \right] \quad (13)$$

746 and

$$\frac{d^2\rho}{dt^2} = \dot{n} = -\frac{3}{a\sqrt{1-e^2}} [T + e(T \cos f + R \sin f)] \quad (14)$$

749 This approach, as explained in [35], as the advantage of  
 750 introducing an element that changes “slowly,” i.e., with a  
 751 time derivative going to zero with the perturbative accel-  
 752 eration. Equations (13) and (14) are comparable in their  
 753 predictions as soon as the perturbing acceleration—in  
 754 particular the  $T$  component—is periodic, i.e., as soon as  
 755 the semimajor axis and the mean motion oscillate around an  
 756 average value. Conversely, the contribution from Eq. (14)  
 757 become predominant if  $T$  is constant, in such a way that  
 758 the changes in mean anomaly accumulate quadratically.

$$\frac{d\Omega}{dt} = \frac{W}{H \sin I} r \sin(\omega + f) \quad (11)$$

718 
$$\frac{d\omega}{dt} = \frac{\sqrt{1-e^2}}{nae} \left[ -R \cos f + T \left( \sin f + \frac{1}{\sqrt{1-e^2}} \sin E \right) \right] - \frac{d\Omega}{dt} \cos I, \quad (12)$$

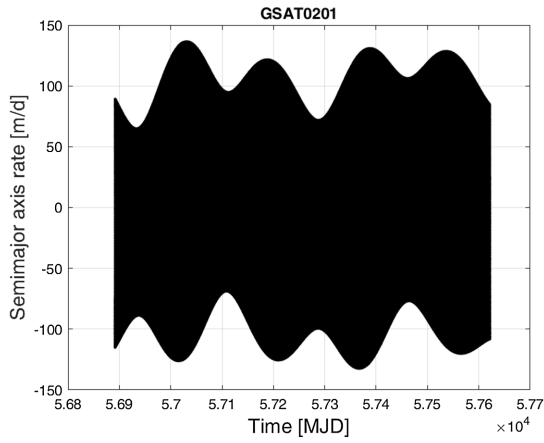
719 where  $r$  represents the satellite distance from the Earth and  
 720  $H$  represents the orbital angular momentum per reduced  
 721 mass of the two-body problem, while  $R$ ,  $T$ , and  $W$  are the  
 722 components of the acceleration in the Gauss form along the  
 723 radial, transversal and out-of-plane directions, respectively.  
 724 In these equations the quantities  $a$ ,  $e$ ,  $I$ ,  $\Omega$ , and  $\omega$  are,  
 725 respectively, the satellite's semimajor axis, eccentricity,  
 726 inclination, longitude of the ascending node and argument  
 727 of perigee, already introduced. The fast angular variables  $f$   
 728 and  $E$  are the satellite's true anomaly and eccentric  
 729 anomaly, finally  $n$  represents the satellite mean motion  
 730 ( $n = 2\pi/P$ , where  $P$  represents the revolution period see  
 731 Table I). The essence of the method is to write the time  
 732 derivatives of the parameters characterizing the perturbed  
 733 satellite orbit, and then numerically integrate them in order  
 734 to find the effects in the elements.

735 Concerning the Gauss equation for a fast variable,  
 736 such as the mean anomaly  $M$ , we have to consider two  
 737 perturbing equations in general. In fact, since the temporal  
 738 variation of  $M$  must be the expression of both the  
 739 perturbative effects and of the mean motion along the  
 740 osculating ellipse, we can introduce two fast variables  $\eta$  and  
 741  $\rho$ , such that  $M(t) = \eta + \rho$  represents the osculating mean  
 742 anomaly at time  $t$  with  $\dot{\rho} = n$ . Finally, for the time variation  
 743 of these two perturbations we obtain:  
 745

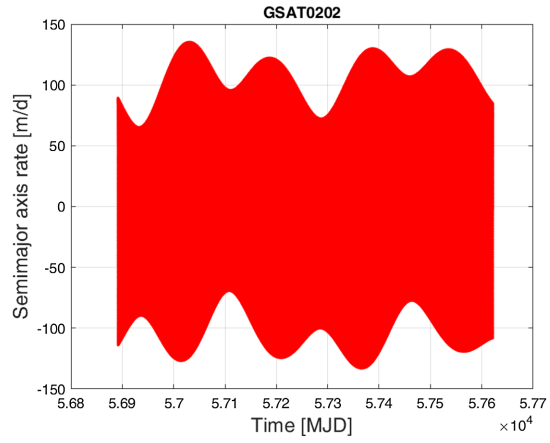
759 We refer to [35] for further details and the complete  
 760 mathematical derivation of Gauss perturbing equations.

761 Figures 19–24 show the results obtained for the  
 762 variation of the six keplerian elements of GSAT0201  
 763 on the basis of our S-BW model and the Gauss perturbing  
 764 equations. The units of measurement are in m/d and 1/d,  
 765 respectively for the rate in the semimajor axis and in the  
 766 eccentricity of the satellites, while they are in rad/d for  
 767 the angular variables.

768 In the case of GSAT0202, only the semimajor axis  
 769 behavior is shown in Fig. 19(b) since, upon first visual  
 770 inspection, the results look identical for the two satellites.  
 771 Of course, they are not exactly the same. The apparent  
 772 overlapping of the results in the different elements arises

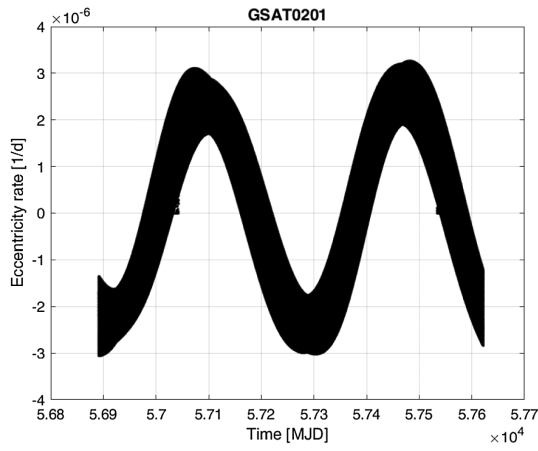


(a)

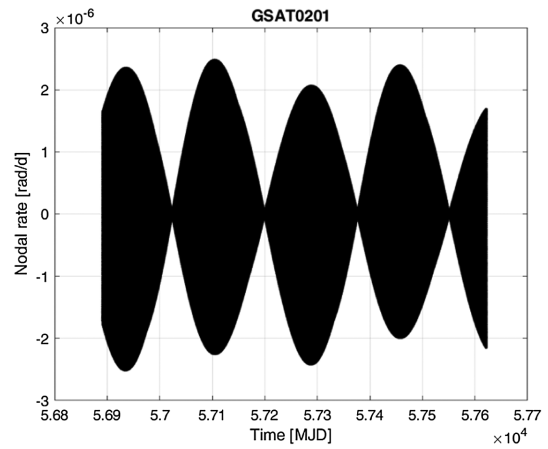


(b)

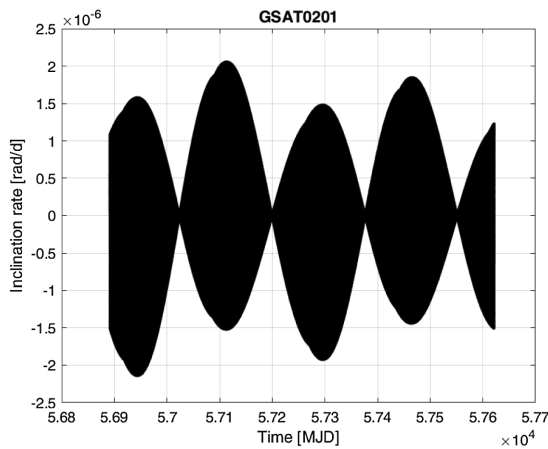
F19:1 FIG. 19. Long-term evolution of the semimajor axis rate of the satellites. (a) GSAT0201: long-term evolution of semi-major axis  
 F19:2 rate  $\dot{a}$ . (b) GSAT0202: long-term evolution of semi-major axis rate  $\dot{a}$ .



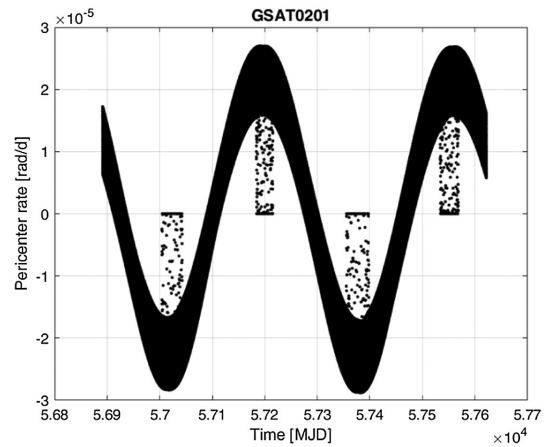
F20:1 FIG. 20. GSAT0201: long-term evolution of eccentricity rate  $\dot{e}$ .



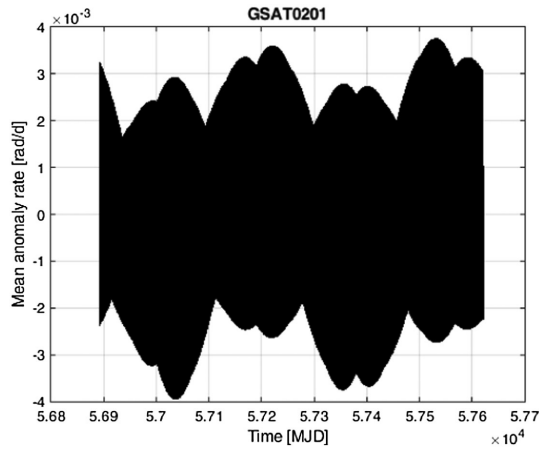
F22:1 FIG. 22. GSAT0201: long-term evolution of the RAAN rate  $\dot{\Omega}$ .



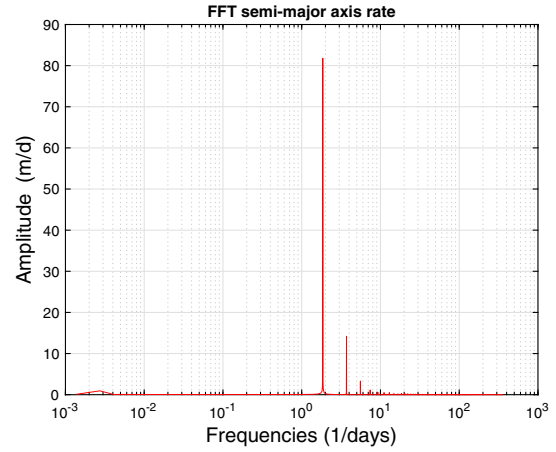
F21:1 FIG. 21. GSAT0201: long-term evolution of inclination rate  $\dot{i}$ .



F23:1 FIG. 23. GSAT0201: long-term evolution of the argument of  
 F23:2 pericenter rate  $\dot{\omega}$ .



F24:1 FIG. 24. GSAT0201: long-term evolution of the Mean anomaly rate in  $\eta$ :  $\dot{\eta}$ .  
F24:2



F26:1 FIG. 26. GSAT0202 (E14): spectral analysis for the rate of the semimajor axis long-period effects of direct SRP.  
F26:2

773 from the fact that the orbits are very close to each other,  
774 practically with the same mean elements and very close  
775 initial conditions, see previous Tables I and IV.

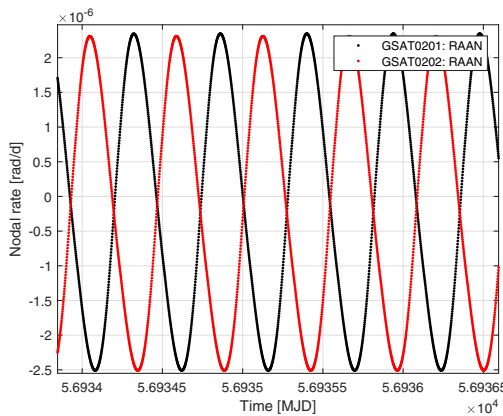
776 The nonoverlapping of the results is evident in Fig. 25,  
777 where the evolution of the rate of the right ascension of the  
778 ascending node (RAAN) and of the rate of the argument of  
779 pericenter for the two satellites are compared over a limited  
780 time interval of some orbits. In the case of the nodal rate,  
781 the evolution is characterized by the same amplitude, but  
782 with opposite phase. Conversely, in the case of the rate of  
783 the argument of pericenter, the behavior is almost in phase  
784 but with different amplitudes.

785 In the case of the mean anomaly variation, see Fig. 24,  
786 we plotted the long-term behavior of  $\dot{\eta}$ , since the variation  
787 in  $\rho$  is comparable because of the behavior of the semimajor  
788 axis rate, mainly characterized by an oscillation at the  
789 orbital frequency, see its FFT for GSAT0202 in Fig. 26.

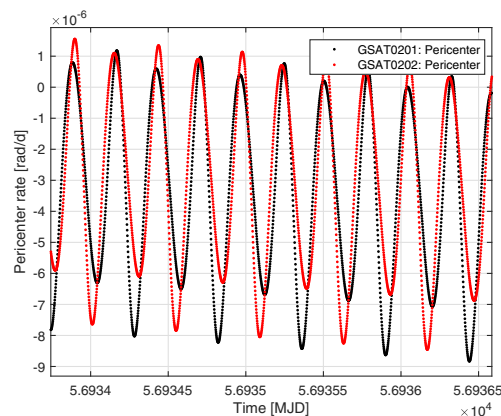
790 Clearly, the short- and long-term periodic effects char-  
791 acterizing the rates of the different orbital elements shown

in the previous figures are those found for the three  
components of Gaussian acceleration further modulated  
by the (fast and slow) angular variables  $f$ ,  $E$ , and  $\omega$  which  
enter the Gauss equations.

In the context of the gravitation measurements of the  
G4S\_2.0 project, in particular as regards the measurement  
of the relativistic precessions of the orbits of the two  
satellites, the long-term behavior obtained for the right  
ascension of the ascending node and for the argument of the  
pericenter are interesting to be analyzed. As can be seen  
from Figs. 22 and 23, integer multiples of a solar year (or  
rather of a draconic period) contain a complete integer  
number of long-period oscillations, i.e., of full cycles.  
This implies that the unmodeled or poorly modeled  
effects of direct solar radiation tend to average toward  
zero (even if not completely) over these time intervals,  
consequently reducing their impact on the estimation of  
systematic errors.



(a)



(b)

F25:1 FIG. 25. Differences in the long-term evolution of the RAAN rate and of the argument of pericenter rate of the satellites.  
F25:2 (a) GSAT0201 and GSAT0202: differences in the long-term evolution of the RAAN rate  $\dot{\Omega}$ . (b) GSAT0201 and GSAT0202: differences  
F25:3 in the long-term evolution of argument of pericenter rate  $\dot{\omega}$ .

TABLE VI. GSAT0201 (E18). Average values in rad/d (first line) and in mas/yr (second line) for the rate of the argument of pericenter  $\dot{\omega}$  on different time intervals of our 2-year analysis.

Element	First 8 months	1st year	2 years	2nd year	Last 8 months
$\langle \dot{\omega} \rangle$	$-8.698 \times 10^{-6}$	$+1.77 \times 10^{-7}$	$+7.0 \times 10^{-8}$	$-3.6 \times 10^{-8}$	$+4.396 \times 10^{-6}$
$\langle \dot{\omega} \rangle$	-655, 291	+13, 335	+5, 274	-2, 712	+331, 187

810 In Table VI, the average value we obtained for the rate of  
 811 the argument of pericenter on five different time intervals  
 812 of our 2-year analysis are shown. Results are provided in  
 813 both rad/d and mas/yr (milli-arc second per year),  
 814 where  $1 \text{ mas/yr} \approx 1.3 \times 10^{-11} \text{ rad/d}$ .

815 From the comparative analysis of this Table with Fig. 23  
 816 it is possible to obtain some useful information in view of  
 817 future measurements in the field of gravitation. The average  
 818 changes by about two orders of magnitude when moving  
 819 from an interval of about 8 months to an interval containing  
 820 a draconic period or two draconic periods. Furthermore,  
 821 even over two different draconitic periods of one year, the  
 822 averages are different, since the maximum positive ampli-  
 823 tudes and the maximum negative amplitudes are different,  
 824 due to the variation of the height of the Sun on the orbital  
 825 plane of the satellite. These average values are huge when  
 826 compared with the smallness of the relativistic precessions  
 827 to be measured, see Table VII. This table shows, respec-  
 828 tively for each satellite, the Schwarzschild (or Einstein)  
 829 precession [43] on the argument of pericenter, the Lense-  
 830 Thirring precession [44] on the RAAN and on the argument  
 831 of pericenter, and finally the de Sitter precession [45] on  
 832 the RAAN.

833 In reality, the values to be considered for the estimation  
 834 of systematic errors are somewhat smaller than those  
 835 indicated in Table VI. Primarily because the SRP will be  
 836 modeled in the software used for the POD of the satellites:  
 837 this would allow the average values to be reduced up to a  
 838 factor of 100 in the case of the FEM. Furthermore, some of  
 839 the parameters that will define our model, whether it is an  
 840 improved BW compared to the current one or a FEM, can  
 841 in turn be estimated thus allowing a further reduction of the  
 842 systematic error to be attributed to our model.

843 Similar considerations apply in the case of the right  
 844 ascension rate of the ascending node. In this case a direct  
 845 measurement of the total relativistic effect is somewhat

TABLE VII. Relativistic precessions on GSAT0201 (E18) and GSAT0208 (E08) and their comparison with LAGEOS II. Units are in mas/yr.

GR precession	GSAT0201	GSAT0208	LAGEOS II
$\dot{\omega}_{\text{Schw}}$	+428.63	+362.72	+3352.58
$\dot{\Omega}_{LT}$	+2.39	+2.18	+31.51
$\dot{\omega}_{LT}$	-5.15	-3.77	-57.33
$\dot{\Omega}_{dS}$	+17.64	+17.64	+17.64

complex and probably unlikely, given the smallness of the  
 relativistic precessions involved, see again Table VII.

## V. PRELIMINARY PODs AND ANALYSIS

848 In this section we introduce the preliminary results of the  
 849 PODs we made for the GSAT0201 and GSAT0208 satel-  
 850 lites. These analysis have been made using GEODYN II [46]  
 851 for the data reduction of the satellites normal points (NPs).  
 852 The modeling setup we are currently using is shown in  
 853 Table VIII. It accounts for: (i) the satellite dynamics, (ii) the  
 854 measurement procedure, and (iii) the reference frames  
 855 transformations. In this context, our models comply,  
 856 wherever possible, with the international resolutions and  
 857 conventions, such as the International Astronomical Union  
 858 (IAU) 2000 Resolutions [47] and the IERS Conventions  
 859 (2010) [42].  
 860

861 Currently, for modeling the spacecraft in the POD we  
 862 have applied a simple cannonball model with an average  
 863 area-to-mass ratio of the Galileo FOC satellite, see Table I.  
 864 The reason for this is twofold. On the one hand, we are  
 865 interested in highlighting in the PODs results the improve-  
 866 ments that are gradually obtained starting from a simple  
 867 satellite model up to the final FEM, via the current S-BW  
 868 model. On the other hand, as already highlighted in  
 869 previous Sec. IV, for the long-term effects we expect that  
 870 even a simplified model will be able to give us significant  
 871 feedback, and our aim is to evaluate how good it is.

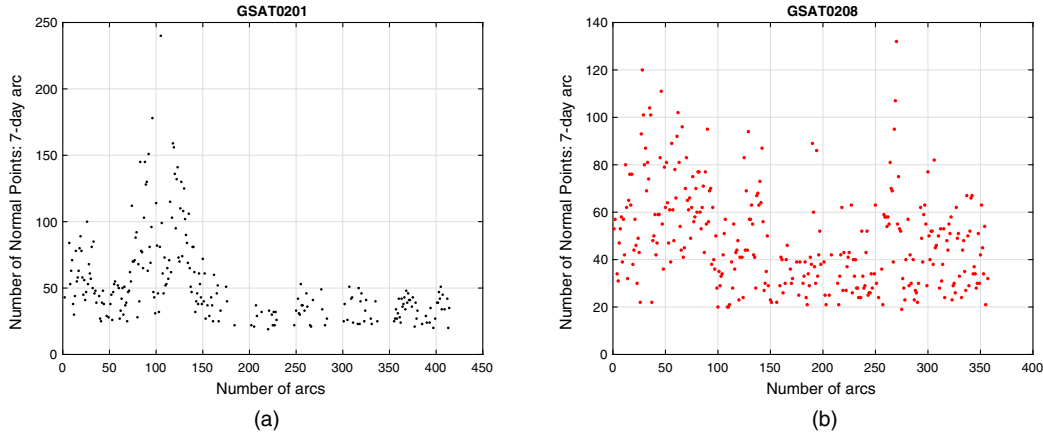
872 The analyzes covered the time interval from the launch  
 873 date of the two satellites, see Table I, until November 25,  
 874 2022: that is, for about 8 years in the case of GSAT0201  
 875 and about 6.8 years in the case of GSAT0208. These time  
 876 intervals were then divided into noncausally connected arcs  
 877 of 7-day for the POD. The POD step size was 50 s.  
 878 Furthermore, to overcome the current excessive simplifi-  
 879 cation of the dynamic model, in particular of the non-  
 880 gravitational forces, empirical accelerations in the form of  
 881 constant and once-per-revolution have been introduced and  
 882 adjusted to absorb part of the mismodeling [66].

883 In Figs. 27–29, the number of observations (NPs), the  
 884 weighted root-mean-square (W-RMS) of the residuals in  
 885 range and the mean of the residuals in range are plotted for  
 886 each arc of the analyses.

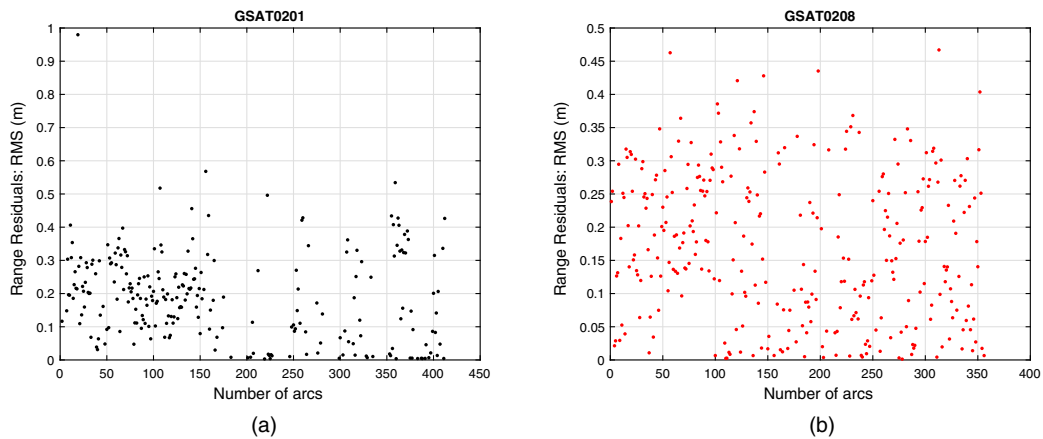
887 The figures allow a first direct comparison of the results  
 888 obtained from the PODs made with GEODYN II in the case of  
 889 a satellite of the Galileo FOC constellation in elliptical orbit  
 890 (GSAT0201, in black) compared with a satellite in nominal  
 891 orbit (GSAT0208, in red). Figure 27 shows us that the

TABLE VIII. Models currently used for the POD obtained from GEODYN II. The models are grouped in gravitational perturbations, nongravitational perturbations and reference frames realizations.

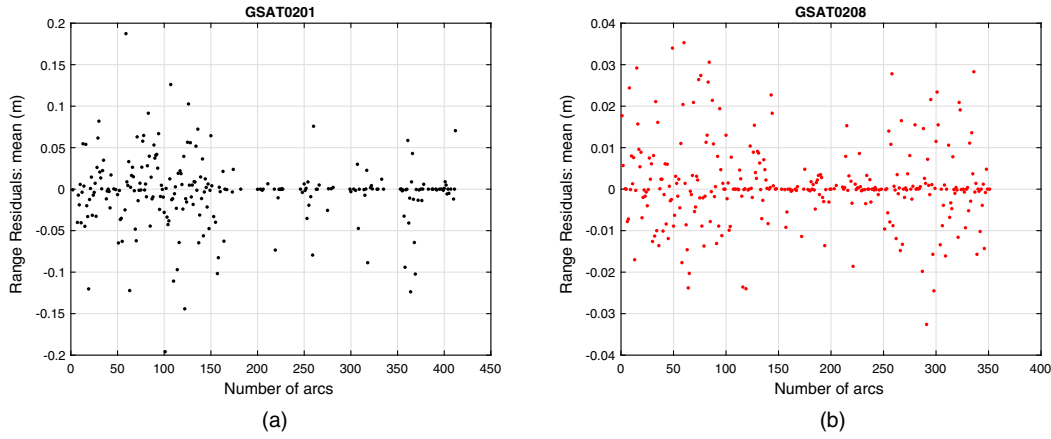
Model for	Model type	References
Geopotential (static)	EIGEN-GRACE02S/GGM05S	[48–50]
Geopotential (time-varying: even zonal harmonics)	GRACE/GRACE FO	[49,50]
Geopotential (time-varying: tides)	Ray GOT99.2	[51]
Geopotential (time-varying: non tidal)	IERS Conventions 2010	[42]
Third-body	JPL DE-403	[52]
Relativistic corrections	Parametrized post-Newtonian	[47,53]
Direct solar radiation pressure	Cannonball	[46]
Earth albedo	Knocke-Rubincam	[54]
Earth-Yarkovsky	Rubincam	[55–57]
Neutral drag	JR-71/MSIS-86	[58,59]
Spin	LASSOS	[60]
Stations position	ITRF2008/2014	[61,62]
Ocean loading	Schernek and GOT99.2 tides	[46,51]
Earth Rotation Parameters	IERS EOP C04	[63]
Nutation	IAU 2000	[64]
Precession	IAU 2000	[65]



F27:1 FIG. 27. Number of observations per arc. (a) GSAT0201: normal points per arc. (b) GSAT0208: normal points per arc.



F28:1 FIG. 28. W-RMS per arc of the satellites range residuals. Outliers more than three standard deviations from the mean of the W-RMS  
 F28:2 have been removed. (a) GSAT0201: weighted root-mean-square of the range residuals. (b) GSAT0208: weighted root-mean-square of  
 F28:3 the range residuals.



F29:1 FIG. 29. Mean values per arc of the satellites range residuals. Outliers more than three standard deviations from the mean of the range  
 F29:2 residuals have been removed. (a) GSAT0201: mean of the range residuals. (b) GSAT0208: mean of the range residuals.

892 GSAT0208 satellite, although it was launched after  
 893 GSAT0201, has been subject to a greater number of  
 894 observations in the form of NPs than the satellite in  
 895 elliptical orbit. In Table IX we summarize, in the case of  
 896 the two satellites, the total number of normal points and  
 897 their average value per year and per day. The latter value  
 898 was also calculated for the 2016–2017 period of the  
 899 ILRS Campaign for the Galileo gravitational Redshift  
 900 Experiment with eccentric sATellites (GREAT) experiment  
 901 [11,12]. As can be seen, during this 2-year period the  
 902 average number of NPs for GSAT0201 is more than twice  
 903 the average over the entire 8-year period considered.  
 904 Conversely, the bottom line (no-GREAT) gives the average  
 905 number of NPs per day after removing the 2-year period of  
 906 the GREAT analysis with the dedicated SLR campaign.

907 Indeed, this represents a delicate aspect for some of  
 908 our measurements, since in the context of G4S\_2.0 we  
 909 are primarily interested in the analysis of the orbits of  
 910 GSAT0201 and GSAT0202 for the measurements of  
 911 relativistic precessions, starting with the Schwarzschild  
 912 one, the greatest of all. This scarce number of normal points  
 913 for satellites in elliptical orbit is unfortunately present  
 914 despite the mentioned ILRS campaign carried out for the  
 915 GREAT project [67].

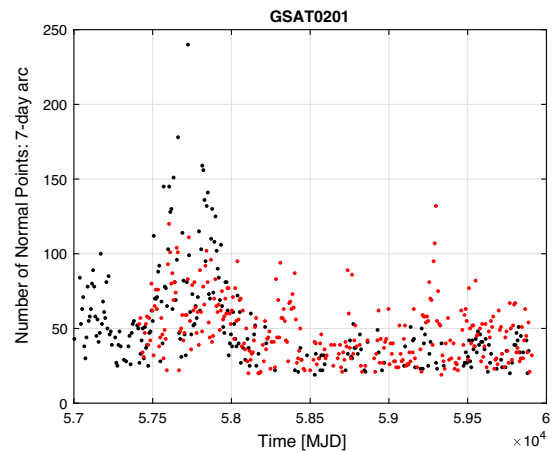
916 In Fig. 30, the NPs of the two satellites are compared  
 917 as a function of time in MJD. In fact, in the period 2016

(MJD 57388)—2017 (MJD 58118), a greater number of  
 918 NPs is clearly seen for the two satellites—in particular for  
 919 the satellite in elliptical orbit—compared to the remaining  
 920 periods, especially from 2018 onward. For this reason we  
 921 asked the ILRS Central Bureau for a new dedicated  
 922 observing campaign for the Galileo FOC satellites to  
 923 improve the number of NPs, in view of the fundamental  
 924 physics measurements of the G4S\_2.0 project.  
 925

926 In particular, we would like to exploit the full-rate data  
 927 during the penumbra transitions to improve the POD during  
 928 these delicate shadow-light transitions, and vice versa, of  
 929 the satellites. Additionally, full-rate data are appropriate for  
 930 determining spacecraft attitude. Therefore, we should try to  
 931 increase the SLR observations under these conditions, at  
 932 least for the two elliptically orbiting satellites, GSAT0201  
 933 and GSAT0202. These two satellites will be used specifi-  
 934 cally for the measurement of the gravitational redshift and  
 935 for the measurement of relativistic precessions. It will be  
 936 anyway useful to also have an increased number of SLR

TABLE IX. Normal Points statistic for GSAT0201 and GSAT0208 on the respective time spans of the analyses performed with GEODYN II.

Normal Points	GSAT0201	GSAT0208
Number of NPs	13,244	15,249
NPs/yr	1661	2235
NPs/d	4.5	6.1
NPs/d (GREAT)	10.9	9
NPs/d (no-GREAT)	2.7	5.1



F30:1 FIG. 30. GSAT0201 (E14) and GSAT0208 (E08): direct  
 F30:2 comparison of the available observations in the NPs format up  
 F30:3 to November 25, 2022.

TABLE X. GSAT0201 and GSAT0208: statistic indicators for the mean of the range residuals (RR) and for their weighted RMS on the respective time spans of the analyses performed with GEODYN II.

GSAT0201	Mean	Standard deviation (cm)
RR	-1.5 mm	8.62
W-RMS	21.44 cm	25.51
GSAT0208	Mean	Standard deviation (cm)
RR	+0.6 mm	1.20
W-RMS	17.30 cm	11.85

937 observations for the other Galileo’s in nominal orbits, to be  
 938 used for the dark matter constraints of the project.

939 Finally, an increased number of SLR data is important to  
 940 reduce systematic errors in the measurements to be per-  
 941 formed. Orbit modeling errors are strongly correlated to the  
 942 clock solutions and SLR data are essential to characterize  
 943 orbital radial errors in the IGS Analysis Centers solutions:  
 944 in fact, the radial systematic errors are one to one correlated  
 945 with the onboard clock solution. Since these systematic  
 946 errors are mainly due to the mismodeling of the direct solar  
 947 radiation pressure, it will be useful to have a campaign long  
 948 enough to account for the variation of the Sun beta angle,  
 949 whose period of variation (as we have seen in Sec. II A) is  
 950 equal to the Draconit year, i.e., very close to 365 days.

951 As mentioned above, in Figs. 28 and 29 the weighted  
 952 root-mean-square (W-RMS) of the residuals in range and  
 953 the mean of the residuals in range are shown for each arc of  
 954 the analyses. The range residuals are defined as:

$$O_i - C_i = -\sum_j \frac{\partial C_i}{\partial P_j} dP_j + dO_i, \quad (15)$$

956 where  $O_i$  and  $C_i$  are, respectively, the range observations  
 957 and their computed (from the dynamical model) values,  
 958  $dP_j$  represent the corrections to the vector  $P$  of parameters

959 to be estimated and, finally,  $dO_i$  are the errors associated  
 960 with each observation. These errors account for both the  
 961 contribution from the noise in the observations as well as  
 962 for the incompleteness of the mathematical model included  
 963 in the software used for the orbit determination. In practice,  
 964 the orbit determination is reduced to the least-squares  
 965 solution of Eq. (15).

966 The scattering of plotted data in these two figures is a clear  
 967 indicator that POD results are suboptimal due to the nonideal  
 968 modeling of NGPs and, in particular, direct solar radiation  
 969 pressure, here provided by a simple cannonball model. This  
 970 is more evident in the case of GSAT0201 in elliptical orbit.  
 971 In Table X we summarized the statistic we obtained for both  
 972 the range residuals and their root-mean-square.

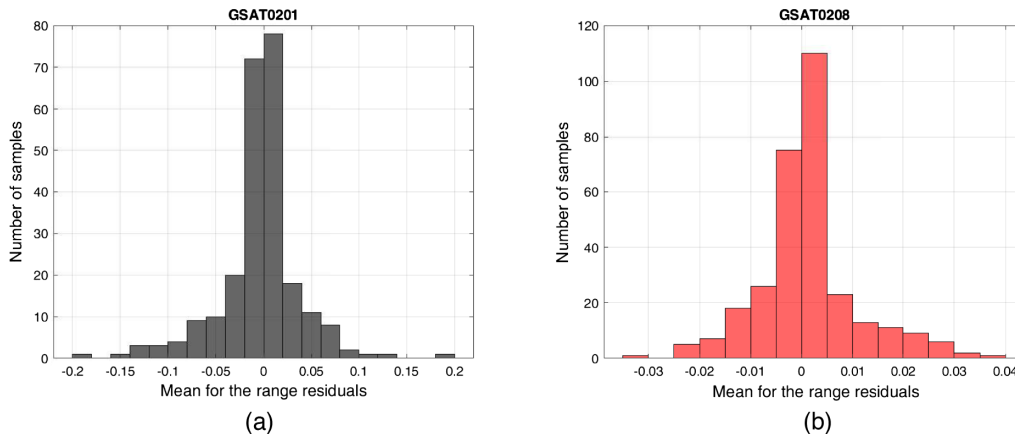
973 As can be seen the mean value of the W-RMS of the  
 974 range residuals is about 20 cm in both cases (with a  
 975 comparable standard deviation), when the POD of satellites  
 976 in nominal orbit is usually at the level of a few cm RMS, or  
 977 even less when carrier phase is used as tracking data [27].  
 978 The fact that the mean value of the residuals in range  
 979 converges toward zero (close to about  $\pm 1$  mm)—and this is  
 980 well highlighted in the histograms of the range residuals of  
 981 the two satellites in Fig. 31—should not mislead.

982 This is due to the use of the previously mentioned  
 983 empirical accelerations, which assume large values after  
 984 data reduction. This is shown below in Figs. 32–34.

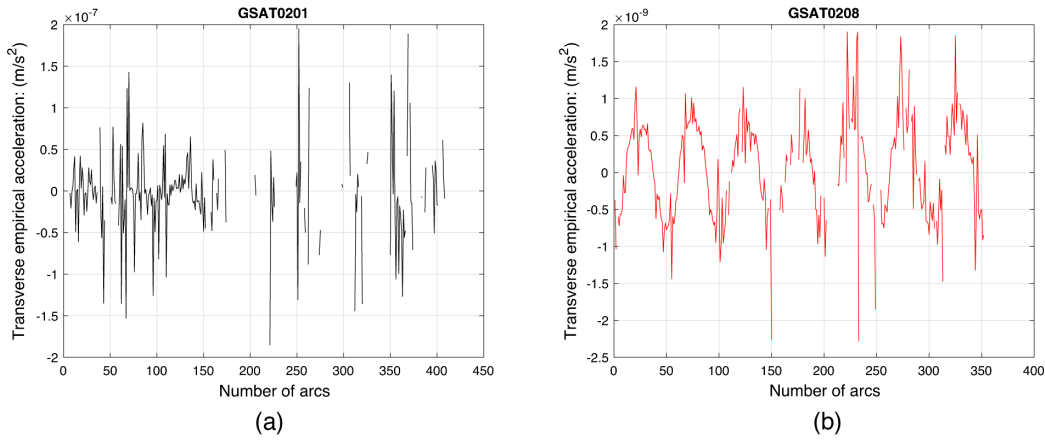
985 These are general acceleration terms added to the equa-  
 986 tions of motion, and are aimed at modeling and/or absorbing  
 987 otherwise unknown small effects which may be relevant for  
 988 the dynamics. In GEODYN II, these acceleration are decom-  
 989 posed in the three Gauss directions under the general form:

$$a(t) = a_0(t) + a_c(t) \cos(\omega(t) + f(t)) + a_s(t) \sin(\omega(t) + f(t)), \quad (16)$$

990 where the amplitudes  $a_c$  and  $a_s$  define the terms of  
 991 acceleration at orbital frequency. In these figures we plotted



F31:1 FIG. 31. Histogram of the range residuals of Fig. 29. (a) GSAT0201: histogram of the range residuals of Fig. 29(a). (b) GSAT0208:  
 F31:2 histogram of the range residuals of Fig. 29(b).



F32:1 FIG. 32. Empirical transverse (constant component) acceleration ( $\text{m/s}^2$ ), estimated for each arc of the POD. Outliers more than three  
 F32:2 standard deviations from the mean of the acceleration values have been removed. (a) GSAT0201: empirical transverse acceleration per  
 F32:3 arc:  $T_0$  constant acceleration. (b) GSAT0208: empirical transverse acceleration per arc:  $T_0$  constant acceleration.

993 the transverse acceleration for the two satellite, the most  
 994 important in defining the shape of the orbit, as can be seen  
 995 from Gauss equations (8) and (9) for the satellite semimajor  
 996 axis and eccentricity.

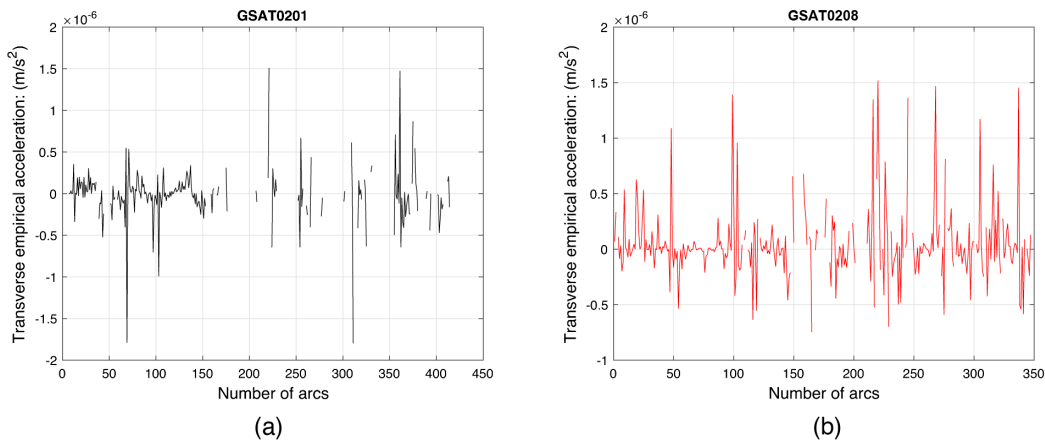
997 From these figures it is once again evident the scarcity of  
 998 the NPs of the satellites, in particular of GSAT0201, clearly  
 999 evident in the arcs in which the data reduction has not been  
 1000 successful (holes in the data). Other information obtained  
 1001 from the plots is the high value of the estimated arc-by-arc  
 1002 amplitudes for the transverse acceleration in the PODs  
 1003 of the two satellites. This is evident from the empirical  
 1004 acceleration terms at orbital frequency, i.e., from the once-  
 1005 per-rev terms  $T_c$  and  $T_s$ , which generally assume ampli-  
 1006 tudes of the order of some  $10^{-7} \text{ m/s}^2$ , i.e., more than one  
 1007 order of magnitude larger than the estimated peak values  
 1008 through our S-BW model, see Sec. III A 2. The situation is  
 1009 better in the case of the constant term for the satellite  
 1010 GSAT0208, whose maximum amplitudes are two orders

of magnitudes smaller than those estimated for 1011  
 the satellite in elliptical orbit. Furthermore, the long-term 1012  
 trend is also well defined, with a periodicity close to the 1013  
 annual one. 1014

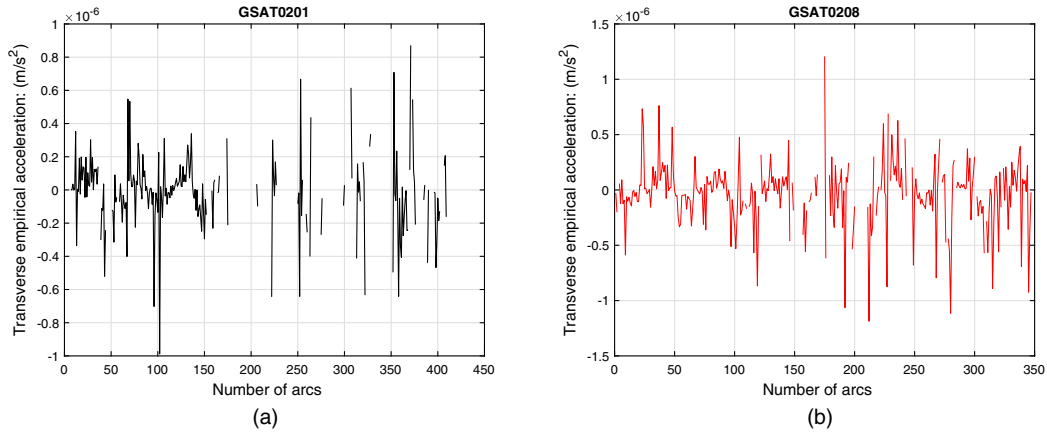
1015 However, in spite of the picture just described, which is  
 1016 not too comforting, if we look at the long-term effects on 1017  
 the orbital elements provided by the cannonball model, the 1018  
 results are somewhat more interesting for our purposes. 1019  
 This will be analyzed in next section.

### A. PODs long-term effects: GSAT0201 1020

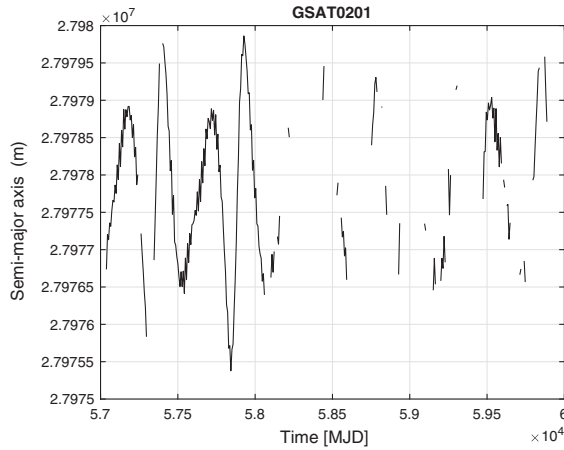
1021 Figures from 35 to 39 show the results obtained for the 1022  
 long-term evolution of the keplerian elements of GSAT0201 1023  
 in elliptical orbit. In Sec. II of the Supplemental Material 1024  
 [39] are reported the results obtained in the case of 1025  
 GSAT0208 in nominal orbit. Specifically, the plotted values 1026  
 represent the adjustment of the state-vector at the start of



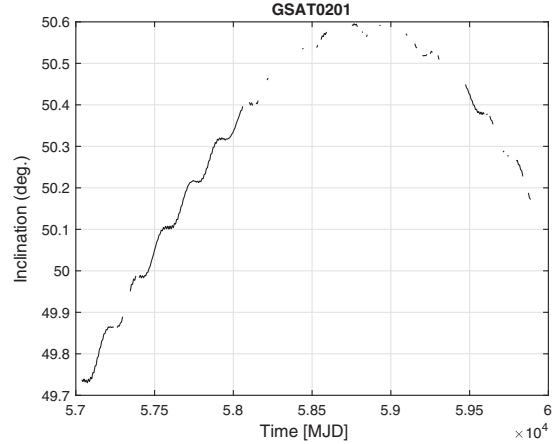
F33:1 FIG. 33. Empirical transverse (cosine component) acceleration ( $\text{m/s}^2$ ), estimated for each arc of the POD. Outliers more than three  
 F33:2 standard deviations from the mean of the acceleration values have been removed. (a) GSAT0201: empirical transverse acceleration per  
 F33:3 arc:  $T_c$  amplitude of the cosine term. (b) GSAT0208: empirical transverse acceleration per arc:  $T_c$  amplitude of the cosine term.



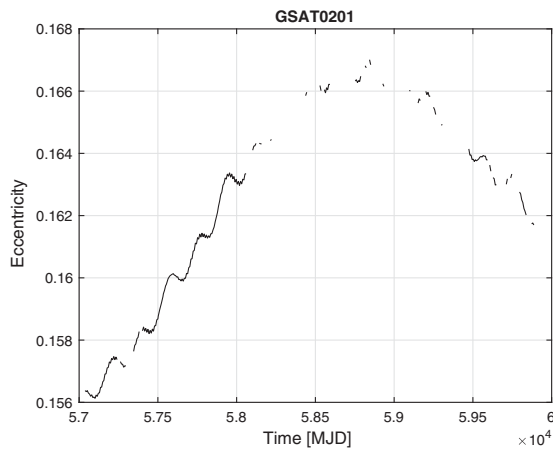
F34:1 FIG. 34. Empirical transverse (sine component) acceleration ( $m/s^2$ ), estimated for each arc of the POD. Outliers more than three  
 F34:2 standard deviations from the mean of the acceleration values have been removed. (a) GSAT0201: empirical transverse acceleration per  
 F34:3 arc:  $T_s$  amplitude of the sine term. (b) GSAT0208: empirical transverse acceleration per arc:  $T_s$  amplitude of the sine term.



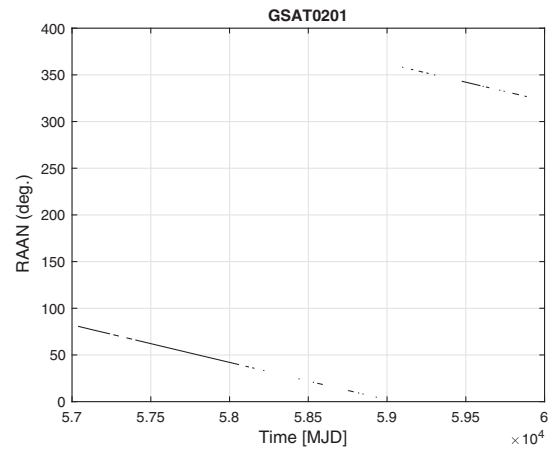
F35:1 FIG. 35. GEODYN II POD of GSAT0201: long-term evolution  
 F35:2 of the semimajor-axis.



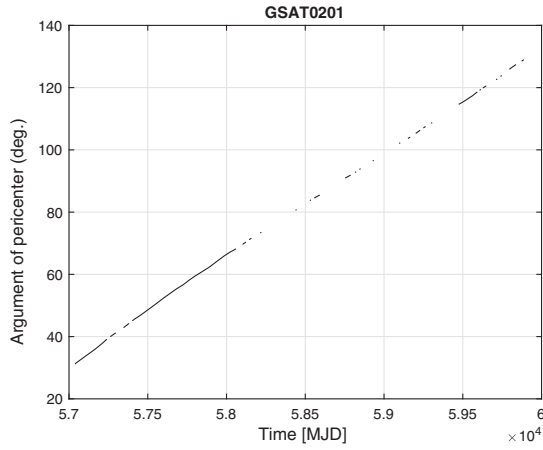
F37:1 FIG. 37. GEODYN II POD of GSAT0201: long-term evolution  
 F37:2 of the inclination.



F36:1 FIG. 36. GEODYN II POD of GSAT0201: long-term evolution  
 F36:2 of the eccentricity.



F38:1 FIG. 38. GEODYN II POD of GSAT0201: long-term evolution  
 F38:2 of the right ascension of the ascending node.



F39:1 FIG. 39. GEODYN II POD of GSAT0201: long-term evolution of  
F39:2 the argument of pericenter.

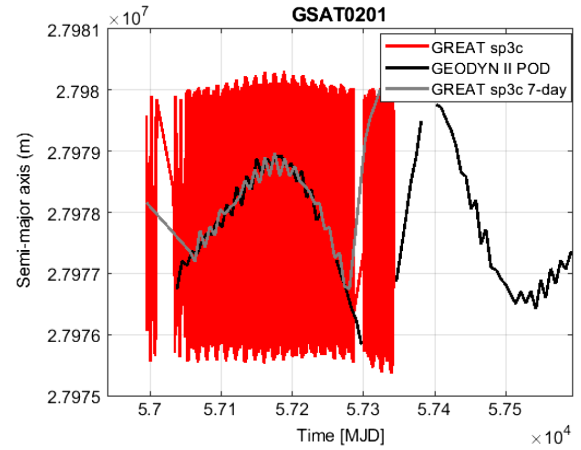


FIG. 40. Comparison between GEODYN II POD (black) and GREAT sp3c precise orbit (red): long-term evolution of the semimajor axis of GSAT0201. F40:1 F40:2 F40:3

each 7-day arc to best fit the available tracking observations of GSAT0201.

As said, the models implemented are those of Table VIII. For the Earth’s background gravitational field we used EIGEN-GRACE02S [48] up to degree and order 30. The initial (a-priori) state-vector for the satellites was obtained from their Two Line Elements (TLE) as provided by NORAD (see [68]).

As we can deduce from these figures, in the case of GSAT0201 the long-term evolution of the orbital elements is different than that of GSAT0208 (see Figs. 7–11 in the Supplemental Material [39]). This is primarily due to the eccentricity of the orbit. In particular, an eccentricity significantly different from zero is responsible for further long- and (also short-) term perturbation effects, starting with the Earth’s gravitational field [69].

In the following we want to compare the results of our PODs with those obtainable from the precise orbits obtained from the IGS analysis centres. In particular, we will compare our PODs with the precise orbits obtained by ESOC for the previous GREAT experiment. The precise orbits, already introduced in Sec. III, are distributed according to the sp3c format. These orbits are the highest quality IGS solutions and consists of daily files produced on a weekly basis.

The results of the comparison in the case of GSAT0201 and GSAT0208 are shown in Figs. 40–44 below and in Figs. 12–16 in the Supplemental Material [39]. Results are shown for the semimajor axis, eccentricity, inclination, right ascension of the ascending node, and argument of pericenter of the satellites. As can be seen from practically all the figures, the agreement on the long-term behavior of the orbits obtained with GEODYN II, based on a simple cannonball model, with those obtained from the sp3c files is quite good. In the case of GREAT, the precise orbits were obtained from ESA’s NAPEOS orbital determination code [70], probably exploiting the dynamic models for nongravitational forces developed within this project.

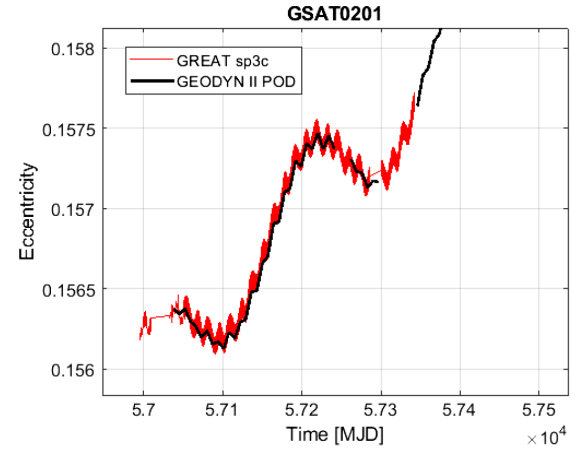


FIG. 41. Comparison between GEODYN II POD (black) and GREAT sp3c precise orbit (red): long-term evolution of the eccentricity of GSAT0201. F41:1 F41:2 F41:3

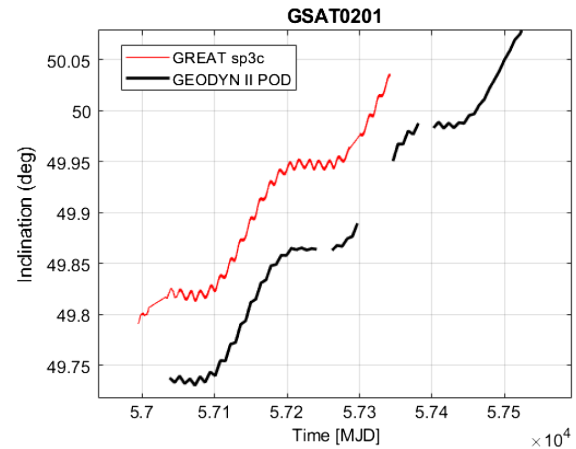
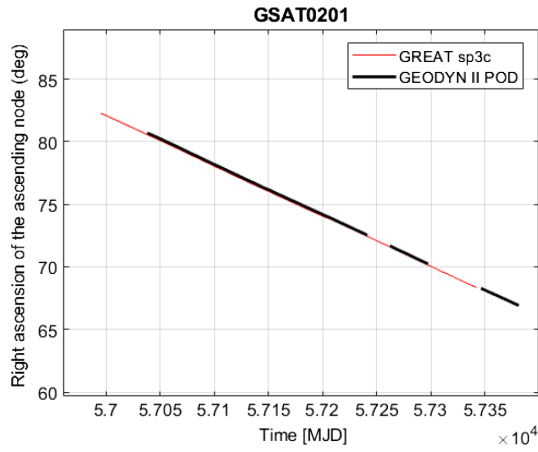
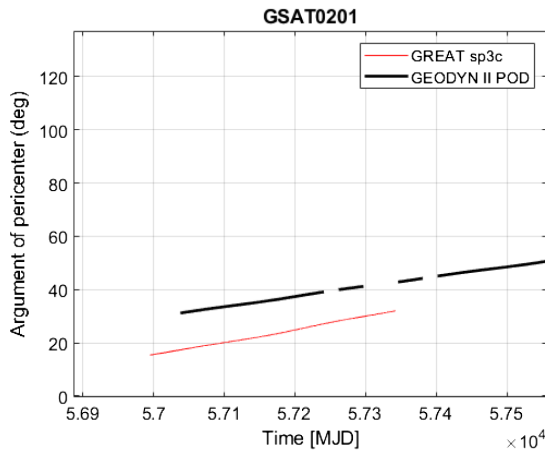


FIG. 42. Comparison between GEODYN II POD (black) and GREAT sp3c precise orbit (red): long-term evolution of the inclination of GSAT0201. F42:1 F42:2 F42:3



F43:1 FIG. 43. Comparison between GEODYN II POD (black) and  
 F43:2 GREAT sp3c precise orbit (red): long-term evolution of the  
 F43:3 RAAN of GSAT0201.



F44:1 FIG. 44. Comparison between GEODYN II POD (black) and  
 F44:2 GREAT sp3c precise orbit (red): long-term evolution of the  
 F44:3 argument of pericenter of GSAT0201.

1065 In both cases, GEODYN II vs GREAT sp3c, the osculating  
 1066 keplerian elements are plotted. One difference lies in the  
 1067 sampling time of the plotted data: 7 days in the case of the  
 1068 POD made with GEODYN II and 300 s in the case of the POD  
 1069 made by ESOC with NAPEOS. This difference is particu-  
 1070 larly evident in the case of the semimajor axis of the orbit of  
 1071 the two satellites considered, but less so in the other cases.  
 1072 For this Keplerian element we plotted the GREAT data  
 1073 sampled every 7 days (gray line). Even in this case the  
 1074 agreement is notable. For some quantities, it was preferred  
 1075 to plot the cumulative sum of the results obtained, as in the  
 1076 case of the right ascension of the ascending node of the two  
 1077 satellites or of the argument of the pericenter in the case of  
 1078 GSAT0201.

1079 In order to begin comparing our POD results with those  
 1080 provided at the high frequencies of the precise orbits  
 1081 obtained by GREAT, we need to reduce the length of  
 1082 our arc and replace the cannonball model with more

sophisticated models, as already anticipated, starting with 1083  
 the S-BW model. 1084

1085 However, the results obtained with the current approxi-  
 1086 mation are nonetheless encouraging as regards the meas-  
 1087 urement of relativistic precessions, linked to the secular  
 1088 effects produced by general relativity (GR)—or by other  
 1089 theories of gravitation (alternatives to GR)—on the right  
 1090 ascension of the ascending node of the orbit and, in  
 1091 particular, on the argument of the pericenter of the  
 1092 satellites. This aspect will be further investigated in the  
 1093 following subsection.

1094 The agreement is remarkable also in the case of the  
 1095 eccentricity of the satellites, as well as for their inclina-  
 1096 tion: the differences are in the values of the initial  
 1097 conditions, in any case less than 0.05 degrees. The  
 1098 extrapolation of the initial condition from the orbits of  
 1099 GREAT is sometimes not easy, as in the case of the  
 1100 argument of pericenter of GSAT0201 but, above all, in the  
 1101 case of the mean anomaly of the satellites, i.e., in the case  
 1102 of a rapidly varying element.

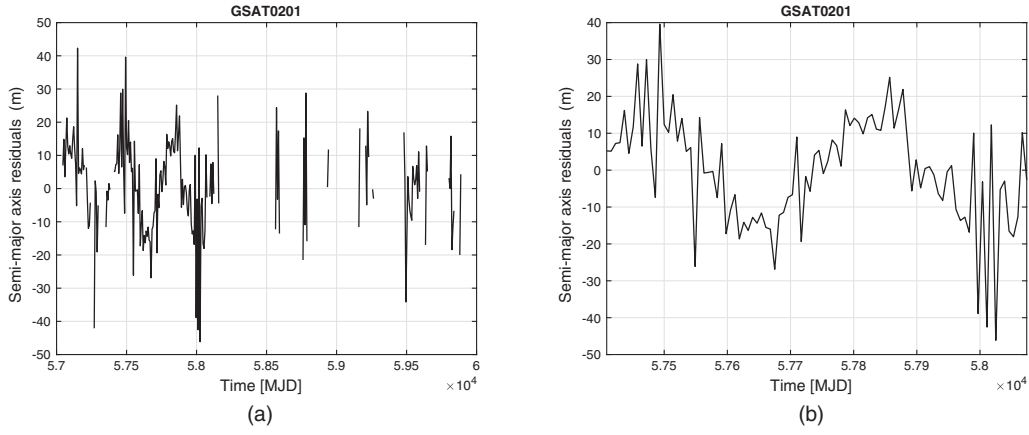
1103 These results give us a clear indication of the possibility  
 1104 of determining, with GEODYN II, the effects of relativistic  
 1105 precessions on the orbit of the Galileo FOC satellites even  
 1106 in the case in which the dynamic model of the satellite is  
 1107 not sophisticated enough, as regards the nongravitational  
 1108 effects. Of course it is necessary to have enough laser  
 1109 observations to ensure state vector convergence in the data  
 1110 reduction process. In the next subsection we will give a first  
 1111 assessment of these aspects in the case of the orbital  
 1112 residuals of GSAT0201.

### B. Orbit residuals in the Keplerian elements 1113

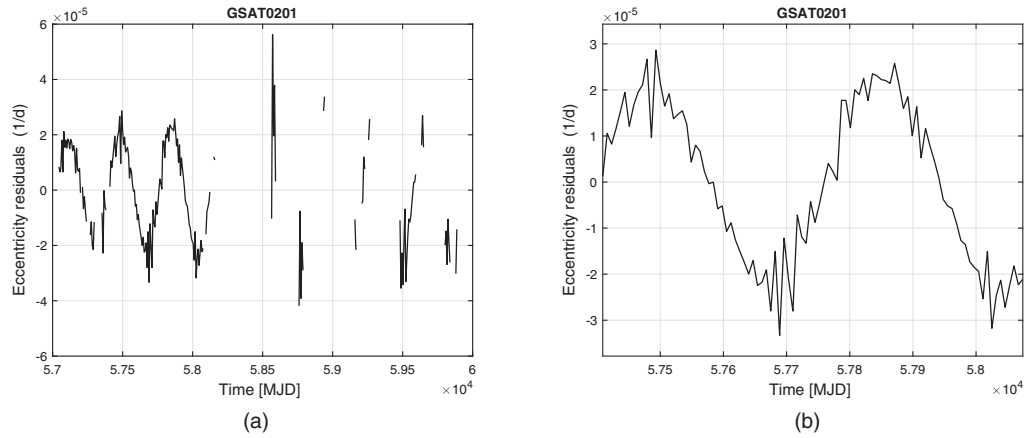
1114 In the following, from Figs. 45 to 50, we show the results  
 1115 for the residuals we obtained from the Keplerian elements  
 1116 of GSAT0201 after a second POD performed by GEODYN  
 1117 II, different from that described in Secs. V and VA. The  
 1118 units of measure for angular quantities are now milliarcsec  
 1119 (mas) per day and not rad/d, as in previous plots.

1120 The two main differences lie in not having modeled  
 1121 general relativity and in not having estimated the empirical  
 1122 accelerations in the POD. This is a correct way, although  
 1123 not the only, to proceed to derive gravitational effects from  
 1124 the analysis of satellite orbital residuals. The model for  
 1125 GEODYN II relativistic corrections refers to the parametrized  
 1126 post-Newtonian (PPN) formalism [71–73] according to the  
 1127 formulation described in [53]. Of course, in this particular  
 1128 case of preliminary POD, the relativistic effects are  
 1129 completely masked by the imperfections of the dynamical  
 1130 model we have used.

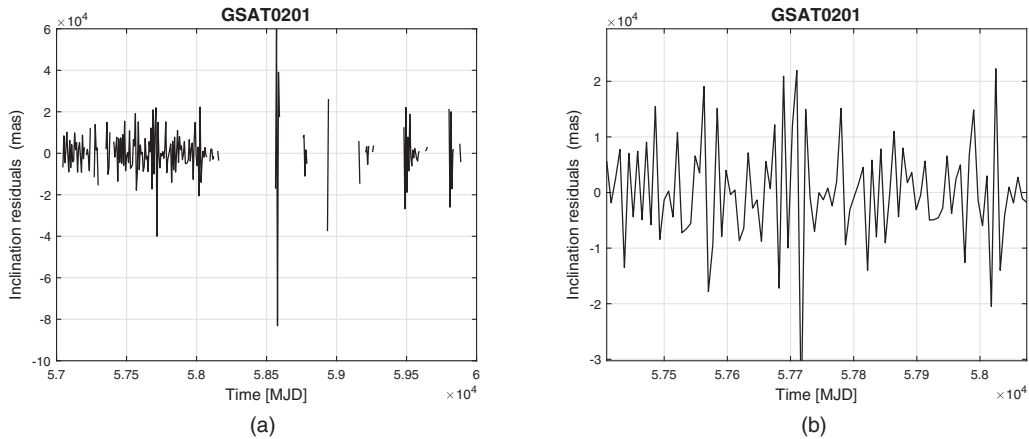
1131 The plotted residuals have been determined with the  
 1132 method described in [74] exploiting the difference between  
 1133 the satellite’s state-vector estimated by GEODYN II at the  
 1134 beginning of each arc of the POD and the propagated value  
 1135 of the (estimated) state-vector of the previous arc at the  
 1136 same epoch. Since the residuals were obtained by



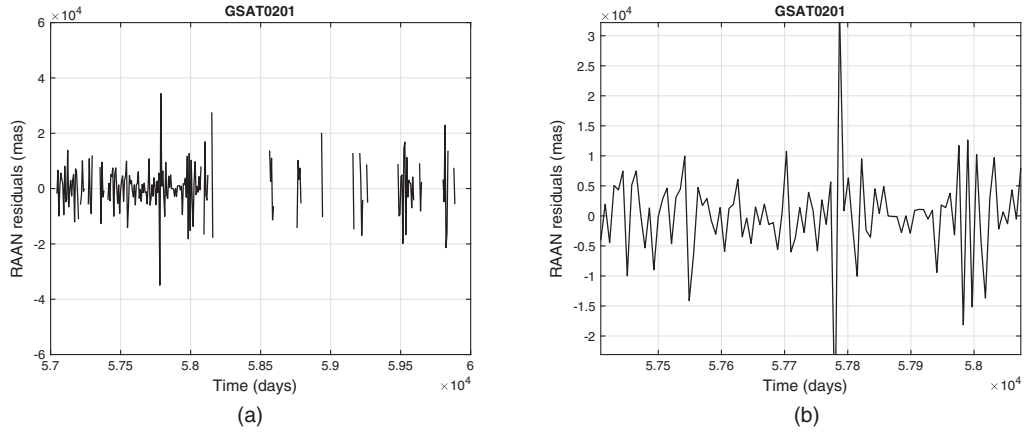
F45:1 FIG. 45. GSAT0201: residuals on 7-day of the satellite’s semimajor axis. (a) GSAT0201: long-term evolution of the satellite’s semi-  
 F45:2 major axis residuals over the entire analysis period. (b) GSAT0201: long-term evolution of the satellite’s semi-major axis residuals in the  
 F45:3 period 2016–2017.



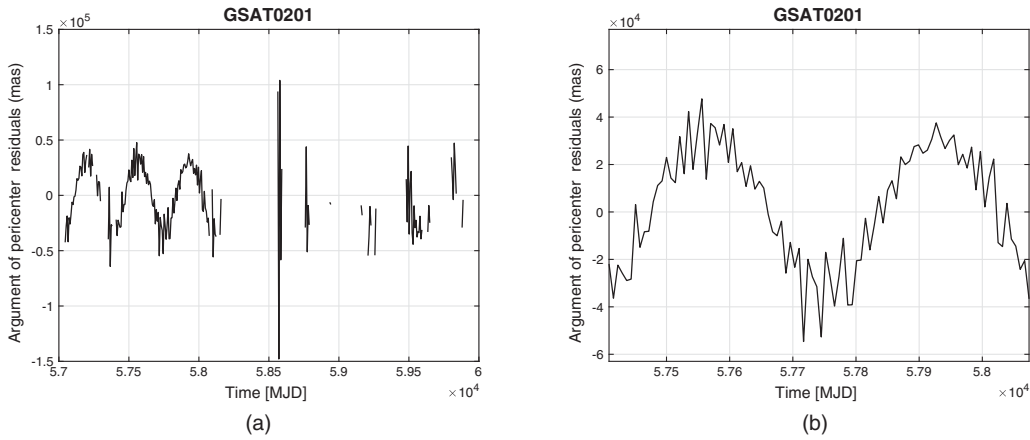
F46:1 FIG. 46. GSAT0201: residuals on 7-day of the satellite’s eccentricity. (a) GSAT0201: long-term evolution of the satellite’s eccentricity  
 F46:2 residuals over the entire analysis period. (b) GSAT0201: long-term evolution of the satellite’s eccentricity residuals in the  
 F46:3 period 2016–2017.



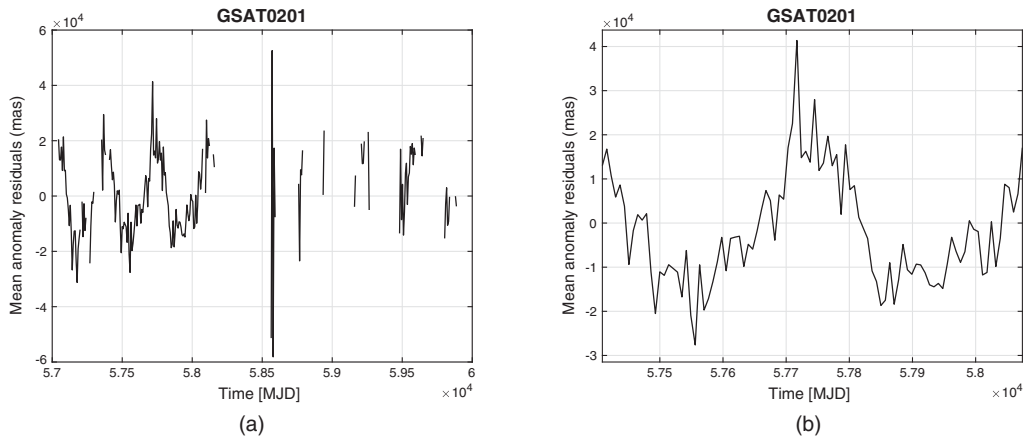
F47:1 FIG. 47. GSAT0201: residuals on 7-day of the satellite’s inclination. (a) GSAT0201: long-term evolution of the satellite’s inclination  
 F47:2 residuals over the entire analysis period. (b) GSAT0201: long-term evolution of the satellite’s inclination residuals in the period  
 F47:3 2016–2017.



F48:1 FIG. 48. GSAT0201: residuals on 7-day of the satellite’s RAAN. (a) GSAT0201: long-term evolution of the satellite’s RAAN residuals  
 F48:2 over the entire analysis period. (b) GSAT0201: long-term evolution of the satellite’s RAAN residuals in the period 2016–2017.



F49:1 FIG. 49. GSAT0201: residuals on 7-day of the satellite’s argument of pericenter. (a) GSAT0201: long-term evolution of the satellite’s  
 F49:2 argument of pericenter residuals over the entire analysis period. (b) GSAT0201: long-term evolution of the satellite’s argument of  
 F49:3 pericenter residuals in the period 2016–2017.



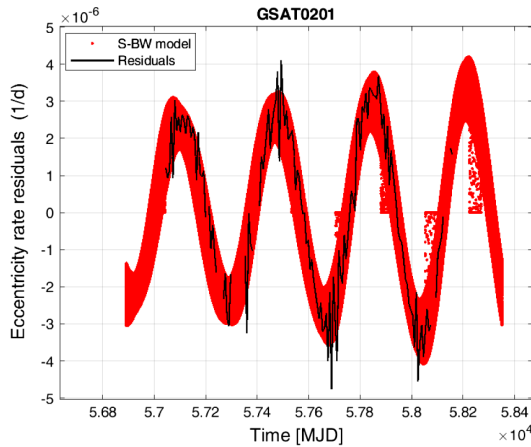
F50:1 FIG. 50. GSAT0201: residuals on 7-day of the satellite’s mean anomaly. (a) GSAT0201: long-term evolution of the satellite’s mean  
 F50:2 anomaly residuals over the entire analysis period. (b) GSAT0201: long-term evolution of the satellite’s mean anomaly residuals in the  
 F50:3 period 2016–2017.

1137 propagating the state vector along the length of each arc,  
 1138 they represent, strictly speaking, the residuals in the rate  
 1139 of the orbital elements, more precisely their variation  
 1140 over 7 days.

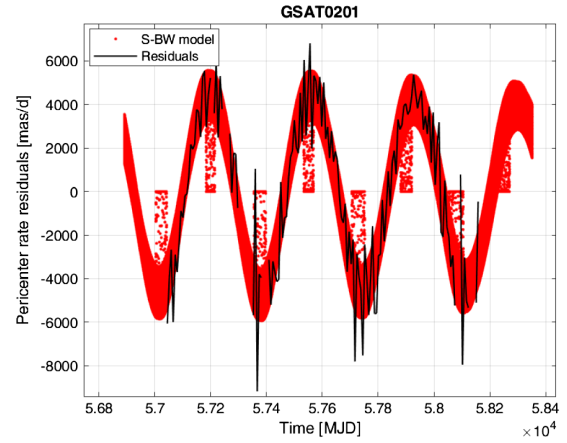
1141 For each figure, the plot on the left shows the residuals  
 1142 over the entire analysis period, i.e., over about 8 years,  
 1143 while the plot on the right shows the residuals we obtained  
 1144 over the 2-year period considered by the GREAT exper-  
 1145 iment: 2016–2017. The residuals plotted over the entire  
 1146 period clearly show the numerous gaps due to the non-  
 1147 convergence of the state-vector during the data reduction  
 1148 because of the scarcity of normal points for this satellite.  
 1149 This was already highlighted in the previous sections.  
 1150 On the contrary, the residuals obtained in the period 2016–  
 1151 2017 do not show any discontinuity, confirming the success  
 1152 of the observational campaign carried out by the ILRS  
 1153 stations in favor of the GREAT experiment in the case of the  
 1154 two satellites in elliptical orbit, see previous Table IX.

1155 As can be seen, most of the figures indicate, in the  
 1156 various orbital residuals, the presence of nonmodeled  
 1157 effects with an annual periodicity. This is less evident in  
 1158 the residuals in inclination and in the right ascension of  
 1159 the ascending node, but it is well evident in all other  
 1160 cases. This is a clear indication of the poor modeling of  
 1161 direct solar radiation for Galileo FOCs in the case of the  
 1162 cannonball model, which on the contrary is a good  
 1163 approximation in the case of passive geodetic satellites,  
 1164 such as LAGEOS [75].

1165 This is indirectly confirmed in Figs. 51 and 52, where the  
 1166 residuals in the eccentricity rate and in the argument of  
 1167 pericenter rate, rescaled per day, are compared with the  
 1168 predictions of our S-BW model presented in Sec. IV  
 1169 (Figs. 20 and 23) and computed on a 4 years period.  
 1170 The S-BW model is in this case able to explain the quasi  
 1171 totality of the residuals currently determined with the POD  
 1172 based on the cannonball model, in particular the annual  
 1173 oscillation.



F51:1 FIG. 51. GSAT0201: direct comparison of the eccentricity rate  
 F51:2 residuals with the corresponding prediction of the S-BW model  
 F51:3 on a 4-year timespan.



F52:1 FIG. 52. GSAT0201: direct comparison of the argument of  
 F52:2 pericenter rate residuals with the corresponding prediction of the  
 F52:3 S-BW model on a 4-year timespan.

1174 These results are remarkable and very important in view  
 1175 of the possibility of extracting the measure of relativistic  
 1176 precessions from the analysis of the orbital residuals of the  
 1177 Galileo FOC satellites.

## 1178 VI. CONSIDERATIONS IN VIEW 1179 OF THE GR MEASUREMENTS

1180 In this section, we will try to summarize, and briefly  
 1181 discuss, the results we have obtained from the analyzes  
 1182 described in this work in the perspective of the next  
 1183 fundamental physics measurements of the G4S\_2.0 project.

1184 The question to ask is how much the model for the  
 1185 nongravitational perturbations of the Galileo FOC satel-  
 1186 lites, and more generally the overall dynamic model of the  
 1187 satellites, needs to be improved in order to achieve reliable  
 1188 measurements for the project’s gravitational measure-  
 1189 ments? Obviously it is not easy to give a clear answer  
 1190 to this question at this stage of G4S.0 activities.

1191 In the following we will restrict our considerations to  
 1192 the measurement of relativistic precessions which, in our  
 1193 planning of the various activities and measurements, should  
 1194 be obtained from the PODs made with the GEODYN II  
 1195 software.

1196 Naturally, the level currently achieved for modeling  
 1197 nonconservative forces and, in particular, direct solar  
 1198 radiation pressure, is not sufficient for a direct measurement  
 1199 of relativistic precessions. For example, in the case of the  
 1200 relativistic precession of the argument of pericenter of  
 1201 GSAT0201—given by the sum of the Schwarzschild and  
 1202 the Lense-Thirring precessions, equal to approximately  
 1203 423.5 mas/yr (see Table VII)—the result should be  
 1204 extracted, for instance, from the average value of the  
 1205 pericenter rate residuals reported in Fig. 49 or 52.

1206 Unfortunately, both the long-term annual oscillation that  
 1207 characterizes the residuals in the rate of the argument of  
 1208 pericenter of the satellite, and the shorter-term ones

1209 superimposed on it, provide an average value that completely  
 1210 masks the prediction provided by GR. Figure 52 shows implicitly that the inclusion of the S-BW model for  
 1211 the satellite in the POD will be able to largely absorb the long-term annual oscillation, but the higher frequency  
 1212 variations shown in the residuals in the pericentric rate will not be certainly absorbed.  
 1213  
 1214  
 1215

1216 These considerations are confirmed by the results of the preliminary activities we have undertaken by including  
 1217 the accelerations obtained with the S-BW model (replacing the cannonball model) in the dynamic model of GEODYN II.  
 1218 This result was achieved by providing two external files to GEODYN II, in binary format, one for the acceleration produced  
 1219 by the SRP on the box-wing model of the satellite and one for the corresponding attitude of the satellite according to the law  
 1220 introduced in Sec. II A.  
 1221  
 1222  
 1223  
 1224  
 1225

1226 Figure 53 provides the results for the residuals of the eccentricity rate and the argument of pericenter rate (in red)  
 1227 for GSAT0201 obtained using the S-BW model accelerations, compared to previous residuals obtained with the cannonball model (in black).  
 1228  
 1229  
 1230

1231 As can be seen, the improvements in residuals reduction are significant: about a factor of 20, or greater, in the  
 1232 maximum amplitude for the eccentricity rate and about a factor of 3 smaller in amplitude in the case of the argument  
 1233 of pericenter rate. However, these improvements are not sufficient to “easily” allow the extraction of relativistic  
 1234 precessions. Indeed, the new residuals in the rate of the argument of pericenter argument are still characterized by a  
 1235 long-term oscillation with annual periodicity, in addition to the expected high-frequency oscillations. From the new  
 1236 analyses, which will be the subject of a dedicated work, we have preliminarily estimated that the residual annual  
 1237 oscillation is due to a transversal acceleration of such periodicity and maximum amplitude of the order  
 1238 of  $1.5 \times 10^{-8} \text{ m/s}^2$ .  
 1239  
 1240  
 1241  
 1242  
 1243  
 1244  
 1245

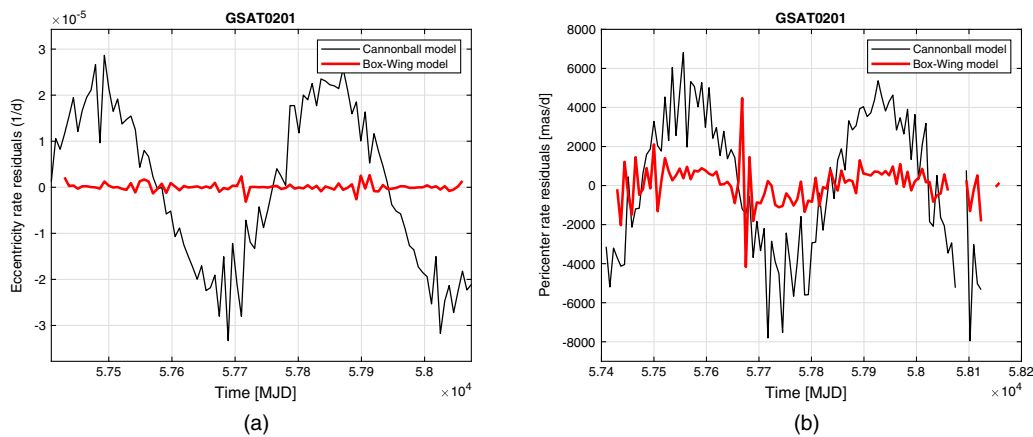
1246 Consequently, as highlighted in previous Secs. III and IV, it will be necessary to further improve the model  
 1247 of the spacecraft to be used for calculating the effects of solar radiation pressure. The first step will be to achieve an  
 1248 improved box-wing model based on a more detailed characterization of the optical properties of the satellite  
 1249 face that constantly looks toward the ground. Then, as a second step, proceed further toward the improvement of the  
 1250 FEM model introduced in Paper I.  
 1251  
 1252  
 1253  
 1254

1255 Only after these improvements in the SRP model, which can be estimated approximately to be a factor of 100 or 200  
 1256 in the orbital residuals compared to the cannonball model, will it make physical sense to take into account the  
 1257 perturbative effects due to the albedo and infrared radiation of terrestrial origin.  
 1258  
 1259  
 1260

1261 For instance, the mean value of the residuals of Fig. 53(b) in the case of the S-BW model, is about 30  
 1262 times greater than the prediction of GR for the combined Schwarzschild plus Lense-Thirring precession (and about  
 1263 300 times greater in the case of the cannonball model). This difference compared to the expected value according to  
 1264 GR, although conspicuous, is not to be considered as an insurmountable obstacle and which consequently makes  
 1265 the measurement of relativistic precession impossible.  
 1266  
 1267  
 1268  
 1269

1270 This is for a series of reasons linked, not only to the further development of the perturbative model (here we  
 1271 have the virtuous example of what the GREAT project has done in the case of the new measurement of gravitational  
 1272 redshift), but also to the different modalities with which the relativistic precession can be extracted from the different  
 1273 orbital residuals.  
 1274  
 1275  
 1276

1277 What the residuals in the various orbital elements show is not simply noise superimposed on the relativistic effects  
 1278 to be measured but, mainly, other effects not modeled or poorly modeled in the dynamic model and primarily of a  
 1279 periodic nature. Therefore, by integrating the residuals in the rate of the orbital elements, as for example in the case of  
 1280  
 1281  
 1282



F53:1 FIG. 53. GSAT0201 cannonball model vs S-BW model: residuals on 7-day of the satellite’s eccentricity and argument of pericenter  
 F53:2 rates. (a) GSAT0201: long-term evolution of the satellite’s eccentricity rate over the 2-year of the GREAT analysis (2016–2017).  
 F53:3 (b) GSAT0201: long-term evolution of the satellite’s pericenter rate residuals over the 2-year of the GREAT analysis (2016–2017).

1283 the rate of the argument of pericenter, we will obtain that  
 1284 the periodic effects integrate and remain periodic and  
 1285 overlap with the linear trend of a relativistic nature. The  
 1286 integration process also acts as a filter, hence “mitigating”  
 1287 the effects on the pericenter rate due to higher frequency  
 1288 periodic oscillations. The measurement of the slope will  
 1289 therefore provide the relativistic precession sought, i.e.,  
 1290 what was before the integration in the average of the rate of  
 1291 the orbital element, now is in the slope of the element itself.  
 1292 Of course, it is important that the time step of the  
 1293 analysis is long enough to include an integral number of  
 1294 (possible) unmodeled long-term periodic effects, which  
 1295 then average their effect on the mean of the residuals, or  
 1296 the slope of the integrated residuals, to zero. As regards  
 1297 the possible lack of normal points for the satellites, the  
 1298 measurement of relativistic precessions can still be  
 1299 attempted over a long time span by means of the statistical  
 1300 analysis used in [76].

## 1301 VII. CONCLUSIONS AND RECOMMENDATIONS

1302 We presented some of the ongoing activities at the  
 1303 IAPS/INAF institute in Rome within the G4S\_2.0 project  
 1304 in fundamental physics funded by the Italian Space Agency  
 1305 (ASI). These activities concern, on the one hand, the  
 1306 development of new models to take into account the non-  
 1307 gravitational forces acting on the satellites of the Galileo  
 1308 FOC constellation of the European Space Agency (ESA), on  
 1309 the other, the determination of the orbit of the satellites by  
 1310 means of a least-square fit of the laser-ranged data (of each  
 1311 spacecraft) provided by the ILRS through the SLR technique.

1312 As far as the models are concerned, as a preliminary to  
 1313 the finite element model of the satellite we are developing,  
 1314 we have introduced a box-wing model built on the basis of  
 1315 the metadata provided by ESA (Sec. III and Paper 1). The  
 1316 model has been applied to take into account the perturba-  
 1317 tion produced by direct solar radiation pressure, the largest  
 1318 among all the perturbations produced by nonconservative  
 1319 forces. The model differs in part from those reported in  
 1320 the literature of GNSS satellites in that the visible solar  
 1321 radiation absorbed by the different surfaces that make up  
 1322 the satellite is not modeled, in terms of its instantaneous re-  
 1323 emission. This effect will in fact be treated more properly  
 1324 under the perturbations linked to the effects of thermal  
 1325 thrust. Conversely, and contrary to the models reported in  
 1326 the literature, the complete law on the complex attitude of  
 1327 the satellite was implemented on the basis of the informa-  
 1328 tion provided by ESA in its twofold form: “nominal” and  
 1329 “modified” (Sec. II A). In this context, we have highlighted  
 1330 some differences that arise in applying the attitude law to  
 1331 satellites in nominal orbit—or almost circular orbit  
 1332 (GSAT0208), for which it was built—with its application  
 1333 to satellites in elliptical orbit (GSAT0201). The box-wing  
 1334 model was used to calculate the accelerations produced  
 1335 by solar radiation on the different surfaces of the satellites.  
 1336 The accelerations have been provided in different

1337 representations—in the time domain, in a synoptic view  
 1338 and in the frequency domain—to highlight their different  
 1339 usefulness for our purposes (Sec. III A and Sec. I of the  
 1340 Supplemental Material [39]). Subsequently, the accelerations  
 1341 in the Gauss reference system were exploited to determine  
 1342 the corresponding effects on the Keplerian elements by means  
 1343 of the so-called Gauss perturbation equations (Sec. IV). All  
 1344 these results have been obtained for the two Galileos in  
 1345 elliptical orbit, GSAT0201 and GSAT0202.

1346 As regards the determination of the orbits of the  
 1347 satellites, a series of preliminary PODs were performed  
 1348 using the GEODYN II code and applying it to the GSAT0201  
 1349 (Sec. V) and GSAT0208 (Sec. II of the Supplemental  
 1350 Material [39]) satellites. In this context, a somewhat crude  
 1351 model was deliberately taken for the satellites, that of a  
 1352 cannonball with an area/mass ratio equal to the average  
 1353 one of the Galileo FOC satellites. In the context of the  
 1354 fundamental physics measurements that we are going to  
 1355 make in the near future, a first verification object of our  
 1356 study was to verify if the distribution of the normal points  
 1357 of the laser data is sufficient to obtain the convergence of  
 1358 the state vector. It has therefore been noted that a sufficient  
 1359 number of normal points is not always available to the  
 1360 scientific community, especially for satellites in elliptical  
 1361 orbit. In this regard we have officially requested to the  
 1362 Central Bureau of the ILRS an observation campaign  
 1363 dedicated to the G4S\_2.0 project, as was done in the  
 1364 recent past for the GREAT and GASTON (GALileo Survey  
 1365 of Transient Objects Network) projects. The SLR campaign  
 1366 was approved and began on January 20, 2024. A second  
 1367 verification carried out was to compare the orbits obtained  
 1368 with GEODYN II, again for the GSAT0201 and GSAT0208  
 1369 satellites, with those we can achieve from the *precise orbits*  
 1370 determined by the IGS analysis centers (Sec. VA and  
 1371 Sec. II of the Supplemental Material [39]). In particular, the  
 1372 orbits obtained by ESOC over the two years of the GREAT  
 1373 project were taken into consideration. The verification was  
 1374 positive, in the sense that even the cannonball model is  
 1375 sufficient to obtain the correct long-term behavior of the  
 1376 orbits of the two satellites considered. We then proceeded  
 1377 to compute the orbital residuals from the orbits obtained in  
 1378 the case of GSAT0201 (Sec. VB). Reliable orbital residuals  
 1379 are an important tool for us to extract from their analysis the  
 1380 signature of the relativistic effects we are interested in, such  
 1381 as the relativistic precessions predicted by general rela-  
 1382 tivity. The residuals we obtained have clearly highlighted  
 1383 the shortcomings of the dynamic model used, in particular  
 1384 the presence of long-term effects with a periodicity of about  
 1385 365 days, therefore attributable to an inadequate modeling  
 1386 of the direct solar radiation pressure. To test this con-  
 1387 clusion, we directly compared the residuals in the orbital  
 1388 elements with the predictions of the box-wing model on the  
 1389 same elements. In fact, the box-wing represents for us a  
 1390 first basic model, we have defined it simplified, toward the  
 1391 construction of more performing models, until hopefully

1392 reaching the FEM of the spacecraft. The comparison was  
 1393 not only positive, but remarkable as almost all of the  
 1394 observed and nonmodeled effects can be replicated with  
 1395 the S-BW model. This result is very significant as it will  
 1396 allow us to enter the accelerations produced by our BW  
 1397 model as input data to the GEODYN II software, as well as  
 1398 those that we will obtain in the future from the spacecraft  
 1399 models that we will gradually develop. This will allow a  
 1400 significant improvement of the dynamic model and therefore  
 1401 the subsequent reduction of tracking data in the POD. This  
 1402 last analysis was introduced in Sec. VI in a preliminary form,  
 1403 where the state of the art of our models was discussed in  
 1404 view of the gravitation measurements that we will have to  
 1405 undertake in the near future.

1406 This work, together with Paper 1 presented in this issue,  
 1407 provides a first overview of the activities and preliminary  
 1408 results of the G4S\_2.0 project, which are preparatory to the

actual measurements of fundamental physics. Other activ- 1409  
 ities more related to these gravitational measures will be 1410  
 presented in future specific works. 1411

## ACKNOWLEDGMENTS 1412

This work is part of the G4S\_2.0 project, developed under 1413  
 the auspices of the Italian Space Agency (ASI) within the 1414  
 frame of the Bando Premiale CI COT 2018 085 under the 1415  
 Accordo Attuativo No. 2021 14 HH.0, with co participation 1416  
 of the Italian Institute for Astrophysics (INAF) and the 1417  
 Politecnico di Torino (POLITO). The authors acknowledge 1418  
 the ILRS (international laser ranging service) Central Bureau 1419  
 for supporting the project objectives through a dedicated 1420  
 SLR campaign and for providing high quality laser ranging 1421  
 data of Galileo satellites. Special thanks to Mike Pearlman 1422  
 (Center for Astrophysics, Cambridge, MA, USA). 1423

1424

- 1425 [1] D. M. Lucchesi, M. Visco *et al.*, preceding article, Funda- 1460  
 1426 mental physics measurements with Galileo FOC satellites 1461  
 1427 and the Galileo for Science project. Part I: a 3D-CAD and a 1462  
 1428 box wing for modeling the effects of nonconservative 1463  
 1429 forces, *Phys. Rev. D* **109**, DG13637 (2024). 1464
- 1430 [2] [https://www.gsc-europa.eu/support-to-developers/galileo- 1465](https://www.gsc-europa.eu/support-to-developers/galileo-satellite-metadata#6)  
 1431 satellite-metadata#6. 1466
- 1432 [3] G. Bury, R. Zajdel, and K. Sořnica, Accounting for 1467  
 1433 perturbing forces acting on Galileo using a box-wing model, 1468  
 1434 *GPS Solut.* **23**, 24 (2019). 1469
- 1435 [4] G. Bury, K. Sořnica, R. Zajdel, and D. Strugarek, Toward 1470  
 1436 the 1-cm Galileo orbits: Challenges in modeling of per- 1471  
 1437 turbing forces, *J. Geodes.* **94**, 16 (2020). 1472
- 1438 [5] F. Vespe, D. Lucchesi, A. Tartaglia, G. Delle Monache, R. 1473  
 1439 Peron, E. Rosciano, F. Santoli, and M. Visco, GALILEO for 1474  
 1440 Science project (G4S): An opportunity to perform new 1475  
 1441 measurements in fundamental physics, in *Scientific and 1476*  
 1442 *Fundamental Aspects of GNSS/Galileo. 6th International 1477*  
 1443 *Colloquium, Valencia (Spain)* (European Space Agency, 1478  
 1444 ESA /ESAC, Spain, 2017). 1479
- 1445 [6] F. Vespe, GALILEO for Science project (G4S): Eccentric 1480  
 1446 GALILEO satellites for general relativistic investigations, 1481  
 1447 in *42nd COSPAR Scientific Assembly* (COSPAR, Pasadena, 1482  
 1448 CA, 2018), Vol. 42, pp. H0.5-3-18. 1483
- 1449 [7] D. Lucchesi, G. Delle Monache, R. Peron, E. Rosciano, M. L. 1484  
 1450 Ruggiero, F. Santoli, A. Tartaglia, M. Visco, and F. Vespe, The 1485  
 1451 Galileo for Science (G4S) project: Fundamental physics and 1486  
 1452 space geodesy by the orbit analysis of the Galileo satellites 1487  
 1453 DORESA and MILENA, in *EGU General Assembly 1488*  
 1454 *Conference Abstracts* (EGU, Vienna, Austria, 2018), p. 15185. 1489
- 1455 [8] M. L. Ruggiero, A. Tartaglia, D. Lucchesi, G. Delle Monache, 1490  
 1456 R. Peron, E. Rosciano, F. Santoli, F. Vespe, and M. Visco, 1491  
 1457 Fully relativistic positioning for the Galileo for Science (G4S) 1492  
 1458 project, in *EGU General Assembly Conference Abstracts 1493*  
 1459 (EGU, Vienna, Austria, 2018), p. 12644. 1494
- [9] <https://igs.org/>. 1460
- [10] H. P. Plag, M. Rothacher, M. Pearlman, R. Neilan, and C. 1461  
 Ma, The global geodetic observing system, *Adv. Geosci.* **13**, 1462  
 105 (2009). 1463
- [11] S. Herrmann, F. Finke, M. Lulf, O. Kichakova, D. Puetzfeld, 1464  
 D. Knickmann, M. List, B. Rievers, G. Giorgi, C. Günther, 1465  
 H. Dittus, R. Prieto-Cerdeira, F. Dilssner, F. Gonzalez, E. 1466  
 Schönemann, J. Ventura-Traveset, and C. Lämmerzahl, Test 1467  
 of the gravitational redshift with Galileo satellites in an 1468  
 eccentric orbit, *Phys. Rev. Lett.* **121**, 231102 (2018). 1469
- [12] P. Delva, N. Puchades, E. Schönemann, F. Dilssner, C. 1470  
 Courde, S. Bertone, F. Gonzalez, A. Hees, C. Le Poncin- 1471  
 Lafitte, F. Meynadier, R. Prieto-Cerdeira, B. Sohet, J. 1472  
 Ventura-Traveset, and P. Wolf, Gravitational redshift test 1473  
 using eccentric Galileo satellites, *Phys. Rev. Lett.* **121**, 1474  
 231101 (2018). 1475
- [13] *COMSOL Multiphysics® Reference Manual, Version 5.5*, 1476  
 COMSOL Multiphysics (Burlington, MA, 1998–2019), 1477  
[www.comsol.com](http://www.comsol.com). 1478
- [14] I. Ciufolini and R. Matzner, Non-Riemannian theories of 1479  
 gravity and lunar and satellite laser ranging, *Int. J. Mod.* 1480  
*Phys. A* **07**, 843 (1992). 1481
- [15] D. M. Lucchesi, LAGEOS II perigee shift and Schwarzs- 1482  
 child gravitoelectric field, *Phys. Lett. A* **318**, 234 (2003). 1483
- [16] D. M. Lucchesi and R. Peron, Accurate measurement in the 1484  
 field of the Earth of the general-relativistic precession of 1485  
 the LAGEOS II pericenter and new constraints on non- 1486  
 Newtonian gravity, *Phys. Rev. Lett.* **105**, 231103 (2010). 1487
- [17] D. M. Lucchesi, The LAGEOS satellites orbit and Yukawa- 1488  
 like interactions, *Adv. Space Res.* **47**, 1232 (2011). 1489
- [18] R. March, G. Bellettini, R. Tauraso, and S. Dell’Agnello, 1490  
 Constraining spacetime torsion with LAGEOS, *Gen. Relativ.* 1491  
*Gravit.* **43**, 3099 (2011). 1492
- [19] D. M. Lucchesi and R. Peron, LAGEOS II pericenter 1493  
 general relativistic precession (1993-2005): Error budget 1494

- 1495 and constraints in gravitational physics, *Phys. Rev. D* **89**,  
1496 082002 (2014).
- 1497 [20] B. M. Roberts, G. Blewitt, C. Dailey, M. Murphy, M.  
1498 Pospelov, A. Rollings, J. Sherman, W. Williams, and A.  
1499 Derevianko, Search for domain wall dark matter with atomic  
1500 clocks on board global positioning system satellites, *Nat.*  
1501 *Commun.* **8**, 1195 (2017).
- 1502 [21] Every satellite has also a Nickname: Doresa and Milena for  
1503 GSAT0201 and GSAT0202, Oriana and Andriana for  
1504 GSAT0206 and GSAT0208. Eac nickname corresponds  
1505 with the name of the child who was the winner of the  
1506 Galileo Children’s Drawing Competition on each European  
1507 Member State.
- 1508 [22] See [https://www.gsc-europa.eu/system-service-status/  
1509 orbital-and-technical-parameters](https://www.gsc-europa.eu/system-service-status/orbital-and-technical-parameters).
- 1510 [23] A. Milani and G. F. Gronchi, *Theory of Orbit Determination*  
1511 (Cambridge University Press, New York, 2010).
- 1512 [24] F. Dilssner, T. Springer, G. Gienger, and J. Dow, The  
1513 GLONASS-M satellite yaw-attitude model, *Adv. Space*  
1514 *Res.* **47**, 160 (2011).
- 1515 [25] O. Montenbruck, P. Steigenberger, and U. Hugentobler,  
1516 Enhanced solar radiation pressure modeling for Galileo  
1517 satellites, *J. Geodes.* **89**, 283 (2015).
- 1518 [26] J. Kouba, A simplified yaw-attitude model for eclipsing  
1519 GPS satellites, *GPS Solut.* **13**, 1 (2009).
- 1520 [27] P. Teunissen and O. Montenbruck, *Springer Handbook of*  
1521 *Global Navigation Satellite Systems* (Springer, Cham,  
1522 Switzerland, 2017), 10.1007/978-3-319-42928-1.
- 1523 [28] Y. Bar-Sever and E. Yoaz, A new model for GPS yaw  
1524 attitude, *J. Geodes.* **70**, 714 (1996).
- 1525 [29] F. Riedel and O. Gülmüs, Observations and operational  
1526 aspects on the Galileo attitude and orbit control subsystem  
1527 infra-red radiance variations (2014), p. 3546.
- 1528 [30] O. Montenbruck, R. Schmid, F. Mercier, P. Steigenberger,  
1529 C. Noll, R. Fatkulin, S. Kogure, and A. Ganeshan, GNSS  
1530 satellite geometry and attitude models, *Adv. Space Res.* **56**,  
1531 1015 (2015).
- 1532 [31] Y. Lou, F. Zheng, S. Gu, and Y. Liu, The impact of non-  
1533 nominal yaw attitudes of GPS satellites on kinematic *ppp*  
1534 solutions and their mitigation strategies, *J. Navig.* **68**,  
1535 718734 (2015).
- 1536 [32] C. Rodriguez-Solano, U. Hugentobler, P. Steigenberger, and  
1537 G. Allende-Alba, Improving the orbits of GPS block IIA  
1538 satellites during eclipse seasons, *Adv. Space Res.* **52**, 1511  
1539 (2013).
- 1540 [33] E. Schoenemann ((ESA) private communication).
- 1541 [34] [https://www.gsc-europa.eu/support-to-developers/galileo-  
1542 satellite-metadata##6](https://www.gsc-europa.eu/support-to-developers/galileo-satellite-metadata##6).
- 1543 [35] A. Milani, A. M. Nobili, and P. Farinella, *Non-Gravitational*  
1544 *Perturbations and Satellite Geodesy* (Adam Hilger, Bristol,  
1545 1987).
- 1546 [36] W. Marquis and C. Krier, Examination of the GPS block IIR  
1547 solar pressure model, in *Proceedings of the 13th*  
1548 *International Technical Meeting of the Satellite Division*  
1549 *of The Institute of Navigation* (ION GPS, Salt Lake City,  
1550 2000), pp. 407–415.
- 1551 [37] C. Rodriguez-Solano, U. Hugentobler, and P. Steigenberger,  
1552 Adjustable box-wing model for solar radiation pressure  
1553 impacting GPS satellites, *Adv. Space Res.* **49**, 1113  
1554 (2012).
- [38] J. I. Andrés de la Fuente, Enhanced modelling of  
LAGEOS non-gravitational perturbations, Ph.D. thesis,  
Delft University Press, Sieca Repro, The Netherlands,  
2007.
- [39] See Supplemental Material at [http://link.aps.org/  
supplemental/10.1103/PhysRevD.000.000000](http://link.aps.org/supplemental/10.1103/PhysRevD.000.000000) for results  
relevant to the satellites GSAT0202 and GSAT0208 con-  
cerning, respectively, the application of the simplified box-  
wing model and precise orbit determination.
- [40] O. Montenbruck and E. Gill, *SatelliteOrbits—Models,  
Methods and Application* (Springer, Berlin, 2005).
- [41] [https://ilrs.gsfc.nasa.gov/missions/satellite\\_missions/current\\_  
missions/ga01\\_com.html](https://ilrs.gsfc.nasa.gov/missions/satellite_missions/current_missions/ga01_com.html).
- [42] G. Petit and B. Luzum, *IERS Conventions (2010)*, IERS  
Technical Note 36 (IERS, Frankfurt am Main: Verlag des  
Bundesamts für Kartographie und Geodäsie, 2010).
- [43] A. Einstein, Die Grundlage der allgemeinen Relativitäts-  
theorie, *Ann. Phys.* **354**, 769 (1916).
- [44] J. Lense and H. Thirring, Über den Einfluß der Eigenro-  
tation der Zentralkörper auf die Bewegung der Planeten und  
Monde nach der Einsteinschen Gravitationstheorie, *Phys. Z.*  
**19**, 156 (1918); B. Mashhoon, F. W. Hehl, and D. S. Theiss,  
On the gravitational effects of rotating masses: The Thirring  
Lense papers, *Gen. Relativ. Gravit.* **16**, 711 (1984).
- [45] W. de Sitter, On Einstein’s theory of gravitation and its  
astronomical consequences. Second paper, *Mon. Not. R.*  
*Astron. Soc.* **77**, 155 (1916).
- [46] D. E. Pavlis *et al.*, *GEODYN II Operations Manual* (NASA  
GSFC, Greenbelt, 1998).
- [47] M. Soffel, S. A. Klioner, G. Petit, P. Wolf, S. M. Kopeikin, P.  
Bretagnon, V. A. Brumberg, N. Capitaine, T. Damour, T.  
Fukushima, B. Guinot, T.-Y. Huang, L. Lindgren, C. Ma,  
K. Nordtvedt, J. C. Ries, P. K. Seidelmann, D.  
Vokrouhlický, C. M. Will, and C. Xu, The IAU 2000  
resolutions for astrometry, celestial mechanics, and metro-  
logy in the relativistic framework: Explanatory supplement,  
*Astron. J.* **126**, 2687 (2003).
- [48] C. Reigber, R. Schmidt, F. Flechtner, R. König, U. Meyer,  
K.-H. Neumayer, P. Schwintzer, and S. Y. Zhu, An  
Earth gravity field model complete to degree and order  
150 from GRACE: EIGEN-GRACE02S, *J. Geodyn.* **39**, 1  
(2005).
- [49] B. D. Tapley, F. Flechtner, S. V. Bettadpur, and M. M.  
Watkins, The status and future prospect for GRACE  
after the first decade, in *Eos, Transactions American*  
*Geophysical Union Fall Meeting Suppl. Abstract G32A-01*  
(AGU, San Francisco, CA, 2013).
- [50] M. Cheng, B. D. Tapley, and J. C. Ries, Deceleration in the  
Earth’s oblateness, *J. Geophys. Res.* **118**, 740 (2013).
- [51] R. D. Ray, A global ocean tide model from TOPEX/  
POSEIDON altimetry: GOT99.2, Technical Paper, Report  
No. NASA/TM-1999-209478, Goddard Space Flight  
Center, Greenbelt, Maryland, 1999.
- [52] E. M. Standish, X. X. Newhall, J. G. Williams, and  
W. M. Folkner, JPL planetary and lunar ephemerides,  
DE403/LE403, Technical Report No. JPL IOM 314.10-  
127, 1995.
- [53] C. Huang, J. C. Ries, B. D. Tapley, and M. M. Watkins,  
Relativistic effects for near-earth satellite orbit determina-  
tion, *Celest. Mech. Dyn. Astron.* **48**, 167 (1990).

- 1615 [54] D. P. Rubincam, P. Knocke, V. R. Taylor, and S. Blackwell, Earth anisotropic reflection and the orbit of LAGEOS, *J. Geophys. Res.* **92**, 11662 (1987). 1651
- 1616 1652
- 1617 1653
- 1618 [55] D. P. Rubincam, LAGEOS orbit decay due to infrared radiation from earth, *J. Geophys. Res.* **92**, 1287 1654
- 1619 (1987). 1655
- 1620 1656
- 1621 [56] D. P. Rubincam, Yarkovsky thermal drag on LAGEOS, *J. Geophys. Res.* **93**, 13805 (1988). 1657
- 1622 1658
- 1623 [57] D. P. Rubincam, Drag on the LAGEOS satellite, *J. Geophys. Res.* **95**, 4881 (1990). 1659
- 1624 1660
- 1625 [58] J. O. Cappellari, C. E. Velez, and A. J. Fuchs, Mathematical theory of the Goddard trajectory determination system, NASA STI/Recon Technical Report No. 76N24291, 1976. 1661
- 1626 1662
- 1627 [59] A. E. Hedin, MSIS-86 thermospheric model, *J. Geophys. Res.* **92**, 4649 (1987). 1663
- 1628 1664
- 1629 [60] M. Visco and D. M. Lucchesi, Comprehensive model for the spin evolution of the LAGEOS and LARES satellites, *Phys. Rev. D* **98**, 044034 (2018). 1665
- 1630 1666
- 1631 [61] Z. Altamimi, X. Collilieux, and L. Métivier, ITRF2008: An improved solution of the international terrestrial reference frame, *J. Geodes.* **85**, 457 (2011). 1667
- 1632 1668
- 1633 [62] Z. Altamimi, X. Collilieux, and L. Métivier, ITRF2014: A new release of the International Terrestrial Reference Frame modeling nonlinear station motions, *J. Geophys. Res.* **121**, 6109 (2016). 1669
- 1634 1670
- 1635 [63] C. Bizouard, S. Lambert, G. César, O. Becker, and J. Y. Richard, The IERS EOP 14C04 solution for Earth orientation parameters consistent with ITRF 2014, *J. Geodes.* **93**, 621 (2019). 1671
- 1636 1672
- 1637 [64] P. M. Mathews, T. A. Herring, and B. A. Buffett, Modeling of nutation and precession: New nutation series for nonrigid Earth and insights into the Earth's interior, *J. Geophys. Res.* **107**, 2068 (2002). 1673
- 1638 1674
- 1639 [65] N. Capitaine, P. T. Wallace, and J. Chapront, Expressions for IAU 2000 precession quantities, *Astron. Astrophys.* **412**, 567 (2003). 1675
- 1640 1676
- 1641 [66] This type of orbit modeling is useful when longwavelengths orbit errors, including secular disturbing effects, need to be removed, as well as for long-period resonances and non-gravitational perturbations that are not included in the software dynamical model, as in this case. Experience shows that, while they are useful to improve the fit quality, they can easily bias the estimation of other quantities. See also the discussion in Paper I. 1677
- 1642 1678
- 1643 [67] A further observation campaign of three months was carried out by ILRS for the ESA project called GASTON, for the search for dark matter of galactic origin. 1679
- 1644 1680
- 1645 [68] <https://space-track.org/>. 1681
- 1646 [69] Y. Kozai, The motion of a close earth satellite, *Astron. J.* **64**, 367 (1959). 1682
- 1647 1683
- 1648 [70] T. Springer, NAPEOS mathematical models, and algorithms, Technical Report No. DOPS-SYS-TN-OIOO-OPS-GN, European Space Operations Center (ESA/ESOC), 2009. 1684
- 1649 1685
- 1650 [71] K. Nordtvedt, Equivalence principle for massive bodies. II. Theory, *Phys. Rev.* **169**, 1017 (1968). 1686
- 1651 1687
- [72] C. M. Will, Theoretical frameworks for testing relativistic gravity. II. Parametrized post-Newtonian hydrodynamics, and the Nordtvedt effect, *Astrophys. J.* **163**, 611 (1971). 1688
- [73] C. M. Will and J. K. Nordtvedt, Conservation laws and preferred frames in relativistic gravity. I. Preferred-frame theories and an extended PPN formalism, *Astrophys. J.* **177**, 757 (1972). 1689
- [74] D. M. Lucchesi and G. Balmino, The LAGEOS satellites orbital residuals determination and the Lense-Thirring effect measurement, *Planet. Space Sci.* **54**, 581 (2006). 1690
- [75] C. W. Johnson, C. A. Lundquist, and J. L. Zurasky, The Lageos satellite, International Astronautical Federation Congress, Anaheim, CA, IAF PAPER 76 065 (1976). 1691
- [76] D. Lucchesi, M. Visco, R. Peron, M. Bassan, G. Pucacco, C. Pardini, L. Anselmo, and C. Magnafico, A 1% measurement of the gravitomagnetic field of the Earth with laser-tracked satellites, *Universe* **6**, 139 (2020). 1692